

Thomas Buchsteiner, BSc

**Spectroscopy of cold atoms and molecules prepared
with helium nanodroplets.**

MASTER THESIS

For obtaining the academic degree
Diplom-Ingenieur

Master program of
Technical Physics



Graz University of Technology

Supervisor: Univ.-Prof. Mag. Dr.rer.nat. Wolfgang E. Ernst
Co-Supervisor: Dipl.-Ing. Dr. techn. Florian Lackner

Institute of Experimental Physics

Graz, August 2014

Zusammenfassung

Zusammenfassung kommt hier...

Abstract

Abstract goes here...

EIDESSTATTLICHE ERKLÄRUNG
AFFIDAVIT

Ich erkläre an Eides statt, dass ich die vorliegende Arbeit selbstständig verfasst, andere als die angegebenen Quellen/Hilfsmittel nicht benutzt, und die den benutzten Quellen wörtlich und inhaltlich entnommenen Stellen als solche kenntlich gemacht habe. Das in TUGRAZonline hochgeladene Textdokument ist mit der vorliegenden Masterarbeit identisch.

I declare that I have authored this thesis independently, that I have not used other than the declared sources/resources, and that I have explicitly indicated all material which has been quoted either literally or by content from the sources used. The text document uploaded to TUGRAZonline is identical to the present master's thesis.

Datum / Date

Unterschrift / Signature

Contents

1. Introduction	1
2. Theoretical Background	3
2.1. Helium	3
2.1.1. Zero point energy	3
2.1.2. Superfluidity	4
2.2. Formation of helium droplets	7
2.2.1. The supersonic gas expansion	7
2.2.2. Doping helium clusters	12
2.3. Spectroscopy	13
2.3.1. Atoms	13
2.3.2. Molecules	16
3. Experimental Setup	21
3.1. Source chamber	22
3.2. Pick up chamber	22
3.3. Detection chamber	24
3.4. Measuring methods	24
3.4.1. REMPI-TOF spectroscopy	25
3.4.2. Laser induced fluorescence spectroscopy	26
4. Experimental Results	29
4.1. RbSr Experiments	29
4.2. Au experiments	33
4.2.1. REMPI spectra	35
5. High temperature pick up source for gold	41
5.1. The oven setup	41
5.2. Temperature measurements	43
5.2.1. Mounting the thermocouple	43
5.2.2. Connecting the thermocouple with a Computer	44
5.2.3. Connecting the power supply	45

6. Programming a temperature controller in LabView	47
6.1. Requirements	47
6.2. Documentation of the LabView block diagram	49
6.2.1. Initialize control elements	50
6.2.2. Asynchronous reading from the Datalogger	50
6.2.3. Converting the thermal voltage	50
6.2.4. PID temperature controlling	52
6.2.5. Warm up and conventional operation mode	52
6.2.6. Cool down	53
6.2.7. Frontpanel	53
6.2.8. Known issues	54
7. Summary and Conclusion	57
A. Technical Drawings	59
B. LabView Block Diagrams	61
List of Figures	62
List of Tables	66
Bibliography	68
Acknowledgments	74

CHAPTER 1

Introduction

CHAPTER 2

Theoretical Background

This chapter covers the theoretical background needed to understand the experimental results given in chapter 4. In the following the properties of helium, the supersonic gas expansion, cluster formation and the fundamentals of the pick up process are explained in detail. At the end of this chapter the basics of atomic and molecular denotations are briefly summed up. More informations on a given topic can be found in the literature referenced in the respective sections.

2.1. Helium

Helium plays an important role in our experiments. It occurs in form of two stable isotopes: ^4He and ^3He with a natural abundance of 99.999863% and 0.000137% respectively [1]. Therefore the term "helium" in this thesis refers to ^4He if not stated otherwise. High purity helium is used as a cold matrix to isolate the species we analyze. Advantages of helium are for example its transparency for light from the infrared up to the ultraviolet spectral regime or the fact that interactions with species are very weak (least perturbing matrix). In the following an overview of the physical properties of helium is given.

2.1.1. Zero point energy

It is not possible to solidify helium at normal pressure. It stays liquid starting from the boiling point at 4.2 K down to absolute zero temperature. Pressures as high as 25 bar are needed to reach the solid phase which explains why it was not observed for a long time.

This behavior can be explained via comparing the zero point energies of liquid and solid helium.

The zero point energy is the energy difference between a quantum system in its ground state and the energy the system would have classically at its minimum. It follows from the Heisenberg uncertainty principle (equation 2.1) that the ground state energy of a quantum system is greater than zero, where in contrast, the lowest possible energy of a classical system equals zero.

$$\Delta x \cdot \Delta p \geq \frac{\hbar}{2}. \quad (2.1)$$

The uncertainty principle states, that two not commuting observables cannot be measured simultaneously with arbitrary accuracy. To fulfill equation 2.1 the uncertainties of the position Δx and momentum Δp of the atoms within the liquid phase have to be nonzero. This also results in potential ($E_{pot} \propto x^2$) and kinetic ($E_{kin} \propto p^2$) energies greater than zero. Therefore the ground state energy, defined as $E_{pot} + E_{kin}$, has to be positive and nonzero as well.

It is possible to explain why helium stays liquid under normal pressure via comparing the zero point energies of the liquid and the solid phase. For the solid phase the zero point energy is as high as 7 meV which is equivalent to a temperature of 70 K [2]. The zero point energy of the liquid helium is below this value. Therefore the liquid phase of helium is favored.

Because the zero point energy is a quantum effect, liquid helium is also called a quantum liquid.

The aggregate state of helium at certain conditions (pressure, temperature) can be determined from the p-T phase diagram shown in figure 2.1 [3]. The diagram shows the ambient pressure in bar over the temperature in Kelvin. Note that the phase diagram shows a fourth (superfluid) state in addition to the three expected aggregate states. At normal pressure superfluidity occurs below a transition temperature of about $T_\lambda = 2.18$ K [4].

Because the helium matrices used in our experiments are superfluid, a short overview of this interesting property is given in the following section.

2.1.2. Superfluidity

Superfluidity is a quantum effect and has been observed for ${}^4\text{He}$, ${}^3\text{He}$ [5], para-hydrogen [6] and ${}^6\text{Li}$ [7]. A superfluid state is characterized through unusual properties like a vanishing internal friction, very high heat conductivity and intriguing effects like film flow and the

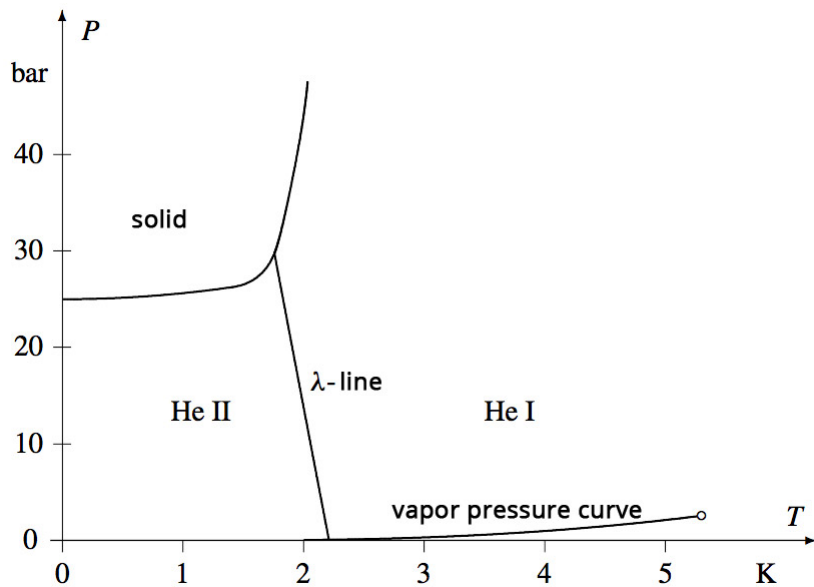


Figure 2.1.: Helium p - T phase diagram showing ambient pressure in bar over temperature in K. The critical point can be identified at 2.2 bar and 5.3 K. The superfluid phase can be observed at normal pressure below temperatures of $T_\lambda = 2.18$ K. Modified from [3].

helium fountain. Superfluidity was discovered by Kapitza in 1938 [8]. Some readers may be interested in the historical paper about the discovery [9].

Normal liquid helium is also called helium I whereas superfluid helium is called helium II. Helium I and helium II are separated through the λ -line which marks a second order phase transition (see figure 2.1). This transition type is characterized by a singularity in its specific heat capacity c_p . Interestingly the transition temperatures of bosonic ^4He ($T_\lambda = 2.18$ K) and fermionic ^3He ($T_\lambda = 3 \cdot 10^{-3}$ K) are very different [4]. This can be understood in terms of ideal bose gases (IBG) and ideal fermi gases (IFG). The description of properties such as superfluidity or superconductivity is based on a macroscopic wave function. This means a macroscopic amount of particles is describable with the same wave function, which is only possible for bosons. In case of superconductivity, electrons (fermions) pair together to form bosons. A very similar mechanism leads to superfluidity of fermionic ^3He , requiring a much lower temperature than ^4He [3]. Note that this mechanism is not a second order phase transition, having other properties than the ^4He phase transition.

Several theories exist to describe the characteristics of superfluidity. A very good overview is given in [3]. Two of those theories, the two-fluid model and the quasi particle model, will be discussed in the following.

The two-fluid model

The two-fluid model by Tisza [10] postulates the liquid helium density as a mixture of a superfluid and a conventional part. Mathematically this can be expressed as

$$\rho = \rho_s(T) + \rho_n(T). \quad (2.2)$$

In formula 2.2 $\rho_s(T)$ represents the density of the superfluid and $\rho_n(T)$ the density of the normal part of the liquid. Both parts are not separated spatially, but are very different in their physical properties. The ratio between the superfluid and the normal part varies with temperature. At absolute zero the superfluid density ρ_s is one in contrast to the transition temperature where ρ_s is zero [3].

The quasi particle model

Another approach is the quasi particle model by Landau [11]. As denoted above, the λ -transition is tightly bound to the theory of ideal bose gases. The quasi particle model uses this theory and describes superfluidity with the possible excitations of particle energies ϵ in an ideal bose gas. The excitations are represented by quasi particles, giving the model its name. Experimentally the elementary excitations are for example observable through inelastic neutron scattering. In that way one can obtain the dispersion relation giving the particle energy ϵ over the wave vector k . The relation is shown in figure 2.2.

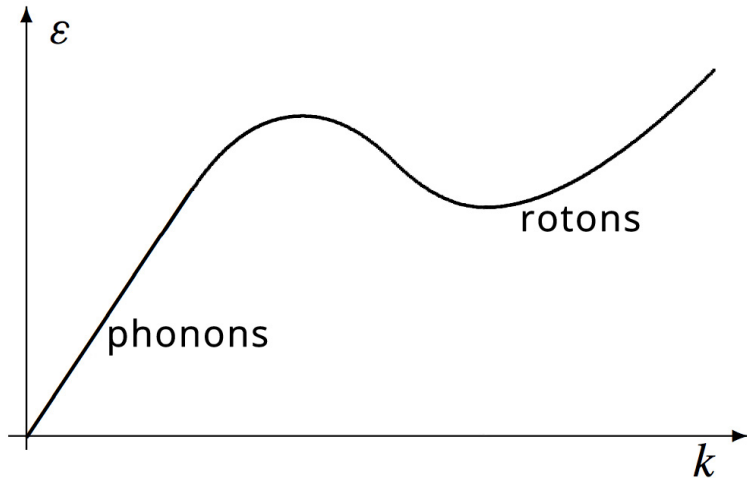


Figure 2.2.: The dispersion relation gives the particle energy over the wave vector. Phonon and roton contributions characterize the dispersion relation at different wave vectors. Taken from [3], modified.

The dispersion relation in figure 2.2 is valid for temperatures $T \lesssim 2\text{ K}$. For very low temperatures ($T < 1\text{ K}$) the behavior is determined by the linear part which results mainly from phonon contributions ($c_V \propto c_{\text{phonons}}$). In this case the specific heat c_V is proportional to T^3 . At temperatures above 1 K the contribution of rottons dominates ($c_V \propto c_{\text{rottons}}$). The name "roton" has developed historically and has no deeper meaning. Within the quasi particle model the specific heat is expressed as the sum $c_V = c_{\text{phonons}} + c_{\text{rottons}}$. In this way the model quantitatively describes superfluidity via the determination of the specific heat. The model does not describe the λ -transition itself [3].

2.2. Formation of helium droplets

This section discusses the process leading to the formation of helium clusters which are used as matrices. Because those clusters are liquid they are also referred to as "droplet". Beside the advantages mentioned in the helium section the droplets also enable the formation of clusters and molecules not observable otherwise. As a result of those remarkable properties Lehmann and Scoles termed the expression "ultimative matrix for spectroscopy" [12].

The helium droplets are build with a method called "supersonic gas expansion" which is explained in the next section.

2.2.1. The supersonic gas expansion

The phase diagram in figure 2.1 shows, that very low temperatures are necessary to condensate helium and form droplets. Condensation sets in when the cooling path crosses the vapor pressure curve. This is called sub critical expansion. The supersonic gas expansion is an adiabatic expansion through a nozzle with high cooling rates and particle velocities partly higher than the local velocity of sound (figure 2.3). The size of the droplets follow a logarithmic normal distribution and their velocities lie within a very narrow distribution [13] [14]. The beam velocity depends on the stagnation conditions and lies between 200 and 400 m/s [4].

To reach the sub critical regime of the phase diagram, the nozzle and the gas are cooled. For gas pressures of about 60 bar the temperature has to be lower than 25 K in order to form droplets [15]. Temperatures of 10 – 16 K are common in our spectroscopic experiments. Pressure and temperature characterizing the expansion are also known as "stagnation conditions".

The nozzle typically has a diameter of about $5 \mu\text{m}$. Gaseous and very pure helium is forced to expand under high pressures into the first vacuum chamber of the apparatus. Common settings are a helium pressure of 60 bar and a vacuum pressure of about 10^{-4} mbar in the source chamber. Figure 2.3 shows the process with different velocity regimes in units of M , the Mach number. As denoted in the graphic, the beam reaches the local velocity of sound at the exit of the nozzle ($M=1$). This is only valid if the ratio between the pressures p_0 and p_a fulfills equation 2.3 (with p_a the background pressure in the source chamber and p_0 the stagnation pressure). In this case the pressure at the nozzle exit becomes independent of p_a .

The ratio between p_0 and p_a is typically in the order of 10^8 . γ is the adiabatic exponent of the gas and is a measure for the expansion due to temperature changes [16]. It is defined as the quotient of specific heat capacity at constant pressure c_p and the specific heat capacity at constant volume c_V . This can also be expressed through the degrees of freedom f of gas particles. For helium, equation 2.5 gives $\gamma = 5/3$.

$$\frac{p_0}{p_a} \geq \left(\frac{\gamma + 1}{2} \right)^{\frac{\gamma}{\gamma - 1}}. \quad (2.3)$$

The zone between nozzle and mach disk is called zone of silence. The zone marks the regime between two points where the beam velocity equals the local velocity of sound.

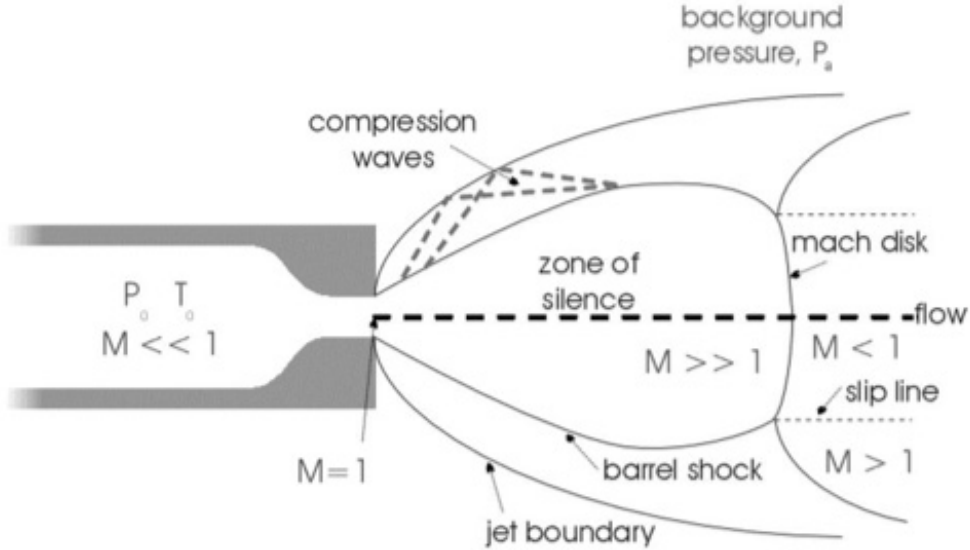


Figure 2.3.: Supersonic gas expansion with different velocity regimes expressed in units of M , the Mach number [17]. The zone of silence marks the regime from the nozzle to the mach disk.

$$a(z) = \sqrt{\gamma \frac{p(z)}{\rho(z)}} \quad (2.4)$$

The local velocity of sound is calculated with formula 2.4 taken from [13]. $p(z)$ and $\rho(z)$ are the pressure and the gas density, respectively. Both depend on the distance z measured from the nozzle exit.

$$\gamma = \frac{c_p}{c_V} = \frac{f + 2}{f} \quad (2.5)$$

In case of a supersonic expansion, fulfilling condition 2.3, the beam expands along the thin, dashed lines in figure 2.3 exceeding the velocity of sound ($M > 1$) at the outer regions of the beam. A higher velocity also means a lower pressure. In fact the pressure

drops under p_a . This causes shock waves (barrel shock), which focus the beam spatially but in turn reduce its velocity to $M < 1$ (inner part of the beam, thin dashed lines). The shock waves travel in beam direction and are separated from regions with $M < 1$ through the Mach disk where $M = 1$. The position of this disk can be calculated with the diameter d of the nozzle via equation 2.6 from [18].

$$z_M = 0.67d \sqrt{\frac{p_0}{p_a}}. \quad (2.6)$$

The distance z_M is measured from the nozzle exit. With the common stagnation conditions ($p_0 = 60$ bar, $p_a = 6 \cdot 10^{-4}$ mbar and $d = 5 \mu\text{m}$) the zone of silence is approximately 3.7 cm long [19].

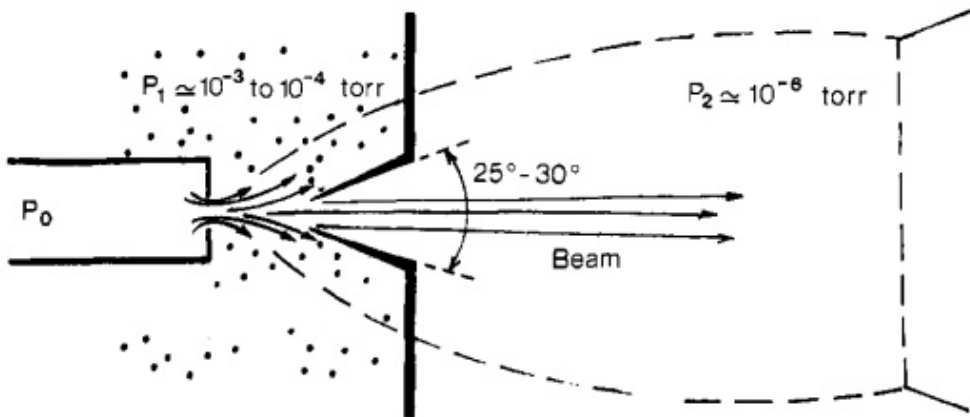


Figure 2.4.: Illustration of the beam extraction with a skimmer. The dashed region is the zone of silence [19].

During the expansion the gas cools down with very high cooling rates of about 10^{11} K/s [20]. Those cooling rates in combination with a pre cooled nozzle enables gaseous helium to condensate and form droplets. A narrow orifice called skimmer ($400 \mu\text{m}$ diameter) extracts the beam. The ideal position for the skimmer depends on the stagnation conditions and can be calculated with

$$z_S = 0.125d \left(\frac{d}{\lambda_0} \frac{p_0}{p_a} \right)^{1/3}. \quad (2.7)$$

z_S is the position of the skimmer and lies within the zone of silence. λ_0 is the mean free path of the particles. An qualitative illustration of the skimmer position is given in figure 2.4 from [19]. Note that the dashed line marks the zone of silence.

After dealing with droplet formation and extraction the following section will provide details about the size distribution of helium droplets.

Droplet temperature and size distribution

During a supersonic gas expansion cooling is caused by particle collisions. After about 1000 nozzle diameters (5 mm) collisions between helium atoms get very rare and the beam consists of helium droplets and single atoms. The droplets within the beam do not grow anymore through condensation, but cooling still takes place due to evaporation of helium atoms. This process cools the droplet to a very stable final temperature (figure 2.5).

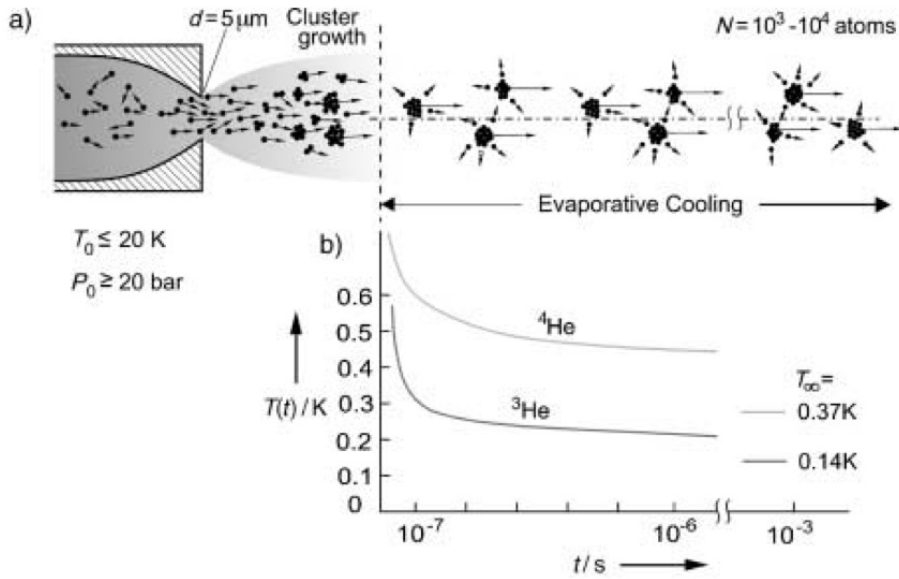


Figure 2.5.: a) Cluster formation within a distance of about 1000 nozzle diameters (5 mm). b) Clusters are cooled further through evaporation of helium atoms. The exponential decay of the cooling rate over time is shown in the diagram. Note that the final temperatures for ${}^3\text{He}$ and ${}^4\text{He}$ are very different. [4]

The droplet temperature was first determined by Goyal, Schutt and Scoles in 1993 [21]. They calculated the temperature from the rotational infrared spectrum of the SF_6 molecule inside a helium droplet. Because the occupation of rotational levels follows a Boltzmann distribution, which is temperature dependent, they were able to determine the temperature from this spectrum. The calculations gave a droplet temperature of 0.37 K, definitely in the superfluid regime of the p-T phase diagram shown in figure 2.1. The high specific heat, which comes with superfluidity, and evaporation cooling are the reasons why this temperature is so stable during experiments. Because the helium droplets are transparent for infrared and ultraviolet light it is not possible to heat them noteworthy with lasers used in our experiments [22].

The cluster size distribution is a logarithmic normal distribution and can be calculated with formula 2.8 taken from [23]. With typical stagnation conditions ($p_0 = 60 \text{ bar}$, $T_{\text{nozzle}} = 15 \text{ K}$) the distribution has its maximum at about 10^4 atoms per cluster. In the formula the average cluster size \bar{N} can be used for the mean value μ and the standard deviation σ can be calculated from the half width $\Delta N_{1/2}$ (see [23]). Note that \bar{N} and

$\Delta N_{1/2}$ are comparable in value as table 2.1 shows.

$$p_N(N) = \frac{1}{\sqrt{2\pi}N\sigma} \exp\left(-\frac{(\ln N - \mu)^2}{2\sigma^2}\right) \quad (2.8)$$

Figure 2.6 taken from ref. [24] shows different distributions for different temperatures. Those distributions were obtained by deflection experiments with a helium pressure of 80 bar. The figure shows that the maximum of a distribution shifts to larger cluster sizes at lower temperatures. Distributions with a maximum at lower cluster sizes show a narrower distribution compared to ones of larger cluster sizes (at lower temperatures).

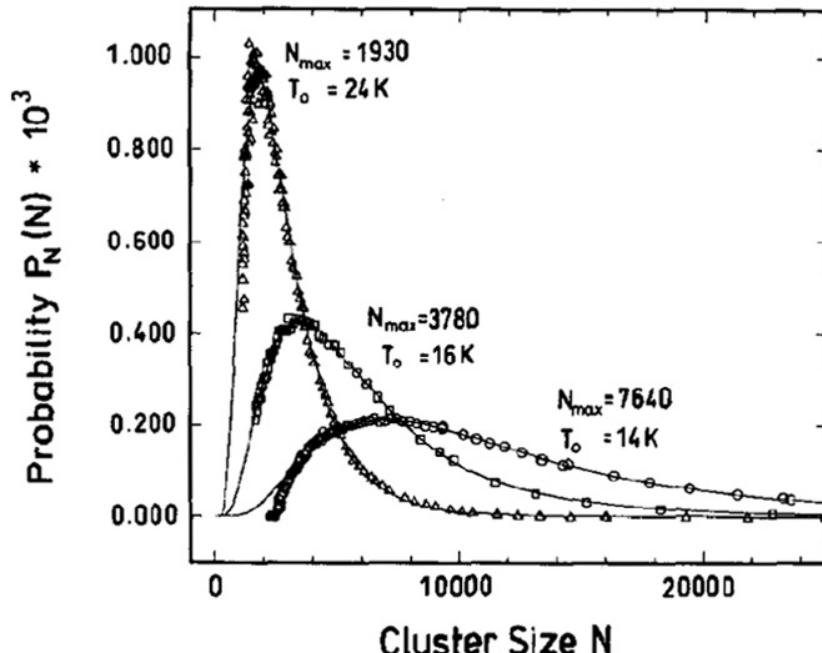


Figure 2.6.: Helium cluster size distribution for $p_a = 80$ bar and different temperatures [24].

Table 2.1.: Typical values for the mean value and the half width of cluster size distributions at different temperatures. [24]

T [K]	\bar{N}	$\Delta N_{1/2}$
24	3170	2670
16	7220	7870
14	14400	15700

The previous sections were dedicated to helium and the formation of droplets. The next important step in our experiments is the pick up process where the helium droplets are doped with the desired species. This pick up process is described in the following section.

2.2.2. Doping helium clusters

Doping describes the process where impurities, in our case the spectroscopically relevant elements, are picked up by the droplet. The pick up takes place in so called "pick up cells". Once the helium droplets enter the cells they collide statistically with gaseous dopants. The probability for a collision increases with the vapor pressure of the dopant. Vapor pressures of about 10^{-4} mbar are sufficient for the pick up process in our experiments. In case of solid species the pressure is controlled via the temperature used to evaporate the dopant. For gaseous species the cell is a cylinder with a gas inlet.

The pick up process follows the Poisson statistics which is defined by

$$P(n|\lambda) = \exp(-\lambda) \frac{\lambda^n}{n!}. \quad (2.9)$$

Formula 2.9 gives the probability to pick up n atoms. λ is the expectation value of pick up processes [25].

Once an atom is picked up it is located within the helium cluster or on its surface [26]. If a second atom is picked up, their long reach van der Waals forces cause attraction between them and dimerization follows. This process is repeated for every atom subsequently added which leads to the formation of clusters of the species. This process takes place in very short time scales of $10^{-8} - 10^{-10}$ s [4]. During the formation, binding energy is set free and causes evaporation of helium atoms. After the molecule is formed and stabilized, helium evaporation cools the system to 0.37 K. In this way the helium droplet works as a personal nanosized cryostat for foreign atoms or molecules. [27]

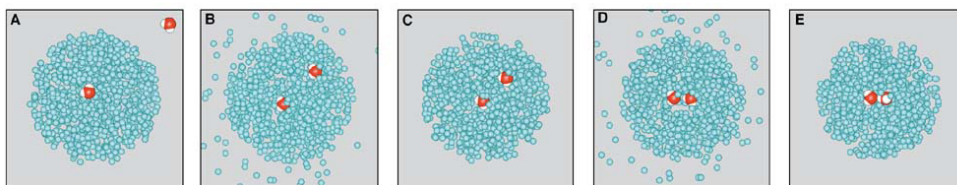


Figure 2.7.: The schematic pick up process and dimerization within a helium cluster. Evaporation caused by a pick up process (B) and due to dimerization (D).[28]

Whether a molecule tends to stay on the surface or to immerse into the droplet can be estimated by the dimensionless Ancilotto parameter λ [29]. It is defined as the ratio between the free energy gain and the free energy cost of forming a cluster inside the helium droplet. The free energy gain is mainly determined by the depth of the pair potential between the dopants and the helium atoms. The free energy cost is proportional to the surface tension of helium. In this way the parameter gives a relative measure of the energy gain associated with the immersed state [29]. For this estimation an infinite impurity mass and a Lennard-Jones pair potential between helium and species are assumed. The formula for the Ancilotto parameter is given in 2.10.

$$\lambda = \frac{\rho\epsilon r_{min}}{\sigma 2^{\frac{1}{6}}} \quad (2.10)$$

ρ is the number density of helium, ϵ and r_{min} are the depth and equilibrium distance of the Lennard-Jones potential well. σ stands for the surface tension of helium. The constant factor $2^{\frac{1}{6}}$ is related to the Lennard-Jones potential. Small values of λ mean that immersion is not favorable. A value of about $\lambda = 1.9$ separates the atoms which stay on the surface from those which immerse [30].

After describing the theoretical basics of helium droplets and the doping process it is now appropriate to deal with spectroscopy.

2.3. Spectroscopy

This section covers the theoretical background for our spectroscopic investigations. It informs about discrete energy levels in atoms and molecules and gives an overview of the spectroscopic annotations used in chapter 4 of this thesis. Due to reasons of simplicity this section will begin with atoms. One and multi electron systems are covered separately for single atoms as well as for the next section about molecules.

2.3.1. Atoms

In case of atoms every state can be characterized with four quantum numbers n , l , s and j . This is only true if no electric or magnetic fields are applied. For all further considerations external fields are neglected.

If quantum numbers are written in lower case letters they describe the state of a single electron whereas quantum numbers in capital letters (L , S , J) describe atomic states. From all atoms the hydrogen atom is the most simple to describe. It has only one valence electron and can be described without electron-electron interactions within a model where energy levels only depend on the principal quantum number n . The different energies are then calculated via formula 2.11. This is equivalent to the Bohr atomic model [25].

$$E_n = -\frac{me^4 Z^2}{2\hbar^2 n^2} \quad n = 1, 2, 3, \dots \quad (2.11)$$

All four quantum numbers n , l , s and j obey several rules. For a given principal quantum number n , only orbital angular momentum quantum numbers $l < n$ are allowed. For every E_n there are $l = 0, 1, 2, \dots, n - 1$ possibilities for the orbital angular momentum quantum

number. Energy levels with a specific l value are denoted with the letters s ($l = 0$), p ($l = 1$), d ($l = 2$), f ($l = 3$),... For hydrogen, energy levels with the same n but different l are degenerated, which means they have the same energy.

To explain the two remaining quantum numbers s and j the electron spin $s = \frac{1}{2}$ has to be taken into account. The electron spin is a quantum mechanical property of an electron and has all characteristics of a classical momentum except that it is not caused by rotation. The sum of electron spin s and orbital angular momentum l results in the total angular momentum $j = l + s$. In that way the state of the single electron and therefore of the hydrogen atom is characterized.

Multiplicity and coupling schemes for atoms with one or more valence electrons

For the general case of one or more electrons L , S and J are introduced and describe the whole atom, not only a single electron. The total spin S for an atom with only one valence electron equals the spin of the single electron $S = \frac{1}{2}$. The different possible orientations of S with respect to L leads to energy splitting of a single level into two states with slightly different energies (for atoms with $L > 0$). To quantify the splitting of energy levels the multiplicity, defined as $2S + 1$, is introduced. For a system with a single electron the multiplicity is two. This reflects the fact, that an electron has two possible spin orientations in the electric field caused by its orbit, namely $s = +\frac{1}{2}$ or $s = -\frac{1}{2}$.

In case of a single electron the total angular momentum J is calculated as $J = |L \pm S|$. For atoms with more than one valence electron the total angular momentum J is determined in two different ways, depending on whether the energy levels are influenced by electron-electron interactions or spin-orbit interactions. Which interaction dominates mainly depends on the atomic number of the atom and therefore on the charge of the nucleus. For atoms with $Z \gtrsim 40$ the spin-orbit interactions dominate. In this case the spin of every electron s_i couples with its orbital angular momentum l_i . Every electron has a total angular momentum $j_i = l_i + s_i$. The total angular momentum of the atom is then $J = \sum_i j_i$. This is known as jj-coupling.

In contrast, light atoms are better described by LS-coupling. Low atomic numbers mean weak spin-orbit interactions. The electron-electron interactions dominate. As a consequence the electrons disturb each other in a way that l_i and s_i do not couple to j_i anymore. In fact all l_i and all s_i couple separately to form $L = \sum_i l_i$ and $S = \sum_i s_i$ respectively. L and S then couple to $J = L + S$.

For those multi electron systems the multiplicity can be higher than two, depending on number and spin alignment of the electrons. States with multiplicity three or four are called triplet or quartet states. States with multiplicity one ($S = 1$) are called singlet.

Spectroscopic denotation of energy states

Every atomic state is denoted with the four already familiar quantum numbers (n , L , S , J) according to the scheme in 2.12.

$$n \ ^{2S+1}L_J \quad (2.12)$$

As a simple example an excited state of helium is given. Helium is a very light atom and can therefore be described by **LS**-coupling.

$$2 \ ^3P_2 \quad (2.13)$$

The excited electron has the principal quantum number $n = 2$. The elevated 3 means that it is a triplet state which can only result from a total spin $S = 1$. There are three possibilities to reach a total spin of one with only two electrons: Both electrons spin-up, both spin-down and one electron up and the other down. Figure 2.8 shows these possibilities graphically.

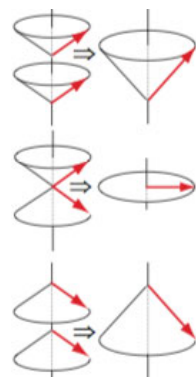


Figure 2.8.: The three possibilities to reach $S = 1$ with two electrons. The resulting spin vectors are different in direction but have the same value. Modified from [31].

This energy splitting is also called fine-structure splitting and is shown graphically for the helium $2 \ ^3P$ level in figure 2.9.

The capital letter P in formula 2.13 refers to the total orbital angular momentum $L = 1$. The index 2 states, that the total angular momentum $J = 2$. In that way the atomic state is defined. Transitions between states are possible and obey certain rules. Those rules are matter of the next section.

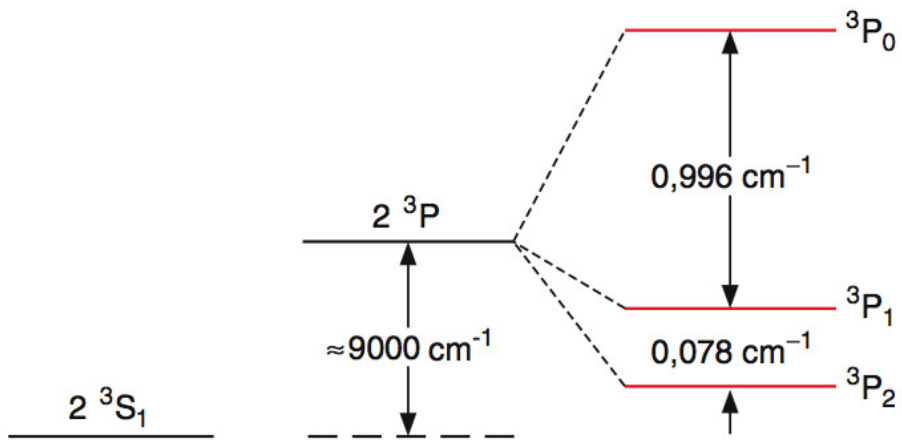


Figure 2.9.: Fine structure splitting of the helium $2\ ^3P$ level into three states with energy differences stated in cm^{-1} . [16]

Selection rules for electronic transitions

Transitions between electronic energy levels can for example be triggered by photons. Following from atomic symmetry considerations, electronic transition rules are introduced. In particular three different selection rules must be fulfilled to allow a transition:

1. $\Delta l = \pm 1$
2. $\Delta j = 0, \pm 1$ (except $j = 0 \rightarrow j = 0$)
3. $\Delta s = 0$

The first rule is equivalent to the conservation of angular momentum (the spin of a photon is 1). The third rule means that multiplicity is also conserved, e.g. forbidding transitions between singlet and triplet systems.

In the next section molecular energy levels and their denotations are described.

2.3.2. Molecules

Spectral lines of free atoms are the result of electronic transitions within the atomic shell. Molecules are groups of two or more atoms held together by chemical bonds. The involved atoms can oscillate relatively to each other or rotate around a specific axis. Additional degrees of freedom make rotations and vibrations possible. In that way not only electronic states but also vibrational and rotational states are available in molecules.

The diatomic molecule

Molecules with two atoms are known as "diatomic molecules". The axis leading directly from one nuclei to the other is called the internuclear axis and is defined as the z-axis. Every electronic state in a diatomic molecule is represented by a potential energy curve. Common energy potentials are the Lennard-Jones or the Morse potential. Figure 2.10 shows the Morse potential (morse) in comparison with the most simplified model, the harmonic oscillator (parabel). The third energy potential (real) in figure 2.10 is the actual potential for Na_2 . The Lennard-Jones and the Morse potential are different mathematical approximations. Especially the Morse potential is often used for modeling diatomic molecules. The harmonic oscillator, as the most simple approach, omits unbound states (it is a parabola with infinite height) and the anharmonic shape of real energy potentials. However it can serve as an approximation for low vibrational states.

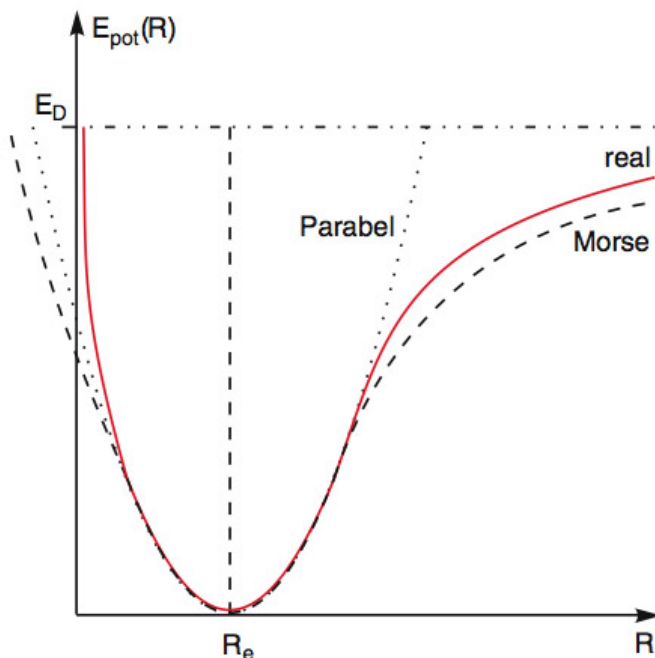


Figure 2.10.: Comparison of harmonic, Morse and a real energy potential (N_2). Modified from [32]

Within each potential energy curve lie various vibrational and rotational states. Vibrational states are usually denoted with ν . The energy difference between neighboring vibrational levels gets smaller for higher energies. To every vibrational level belong several rotational levels. Figure 2.11 illustrates two different electronic states with vibrational and rotational levels (in the gray rectangles).

In diatomic molecules the core field of the two nuclei is cylinder symmetric around the z-axis. This causes a precession of the orbital angular momentum vector ℓ around the internuclear axis. The vector changes over time and ℓ is no longer a conserved quantity. In this section the characteristic quantum numbers for molecules are first introduced for one- and then for multi electron systems. Examples for one electron systems are ions

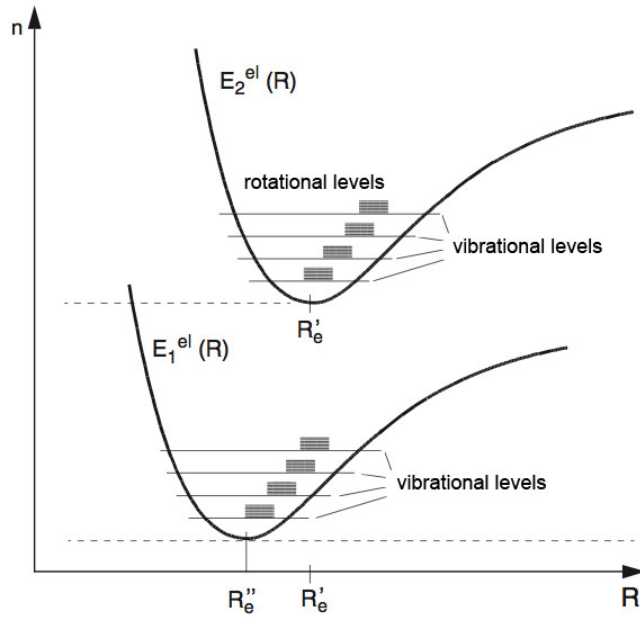


Figure 2.11.: Two electronic states represented by two molecular potentials energy curves with different equilibrium distances R'_e and R''_e . Vibrational and rotational states are drawn within the energy curves. Modified from [33]

like H_2^+ or Li_2^+ . With these quantum numbers the different coupling schemes and the molecular denotation will be described.

One electron systems

In the previous section about atoms we differentiated between two coupling schemes (LS- and jj-coupling). For molecules five coupling schemes, called Hund's case (a)-(e), exist. Which Hund's case the molecule describes best, depends on which interactions influences the molecule the most. Three interactions have to be taken into account: electrostatic, spin-orbit and rotational interactions. For nuclei with low atomic numbers the interactions between ℓ and s are weak. This is described by Hund's case (a). In this case both vectors precess independently around the z-axis. As conserved quantities the two quantum numbers λ and σ are introduced as projections of ℓ and s onto the z-axis. Their values are $\lambda\hbar$ and $\sigma\hbar$. Figure 2.12 illustrates Hund's case (a) for a molecule with one valence electron.

Two and more electron systems

For multi electron systems the angular momenta of the electrons couple. In which way they add up is determined by the kind of dominant interactions and therefore again describable by the hund's cases. The two common Hund's cases (a) and (c) are described in this section. Hund's case (a) is characterized by strong electrostatic interactions whereas strong spin-orbit interactions are described by Hund's case (c). Both cases are illustrated for multi electron systems in figure 2.13.

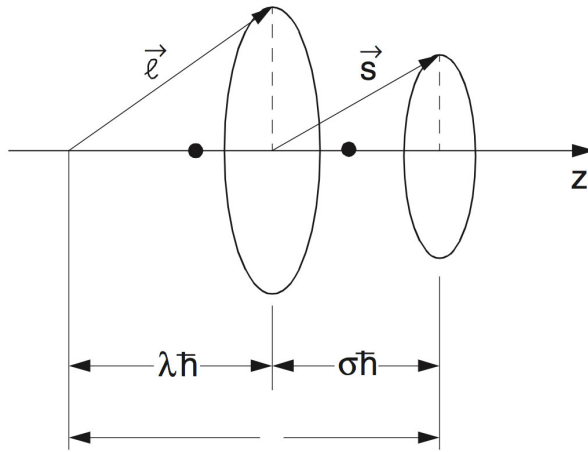


Figure 2.12.: Hund's case (a) for a molecule with one valence electron. ℓ and s are independently precessing. The values of their projections are drawn. From [33]

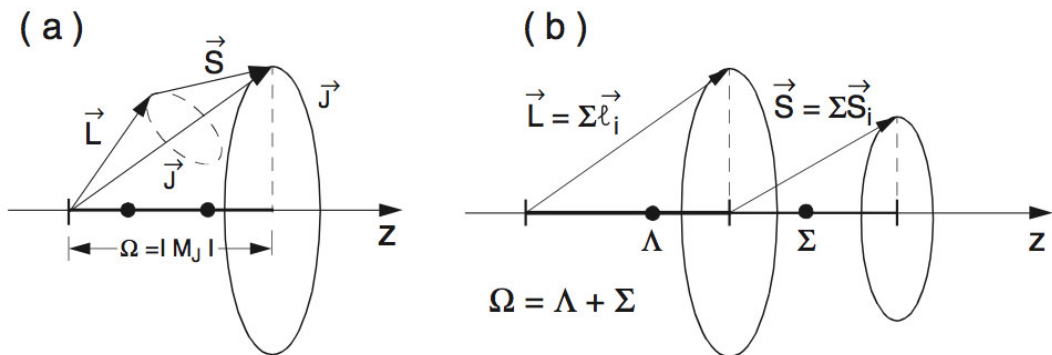


Figure 2.13.: a) Hund's case (c) strong $\mathbf{L} - \mathbf{S}$ interactions. b) Hund's case (a): Independently precessing vectors where the core-field breaks the coupling of \mathbf{L} and \mathbf{S} . From [33]

Figure 2.13 a) shows the coupling of total orbital angular momentum \mathbf{L} and total spin \mathbf{S} in case of strong spin-orbit interactions. Because both vectors are precessing, the total angular momentum $\mathbf{J} = \mathbf{L} + \mathbf{S}$ precesses around the internuclear axis. However, to define a quantum number for the total angular momentum vector, Ω is introduced as the projection of \mathbf{J} onto the z-axis. Its absolute value is called M_J .

$$\Omega = |M_J|, \quad \Omega = J, J-1, \dots, \frac{1}{2} \quad \text{or} \quad 0 \quad (2.14)$$

The second case shown in figure 2.13 b) illustrates the coupling for strong electrostatic interactions, Hund's case (a). The two vectors \mathbf{L} and \mathbf{S} couple separately to the internuclear axis and precess independently. The orbital angular momenta of the single electrons sum up to form $\mathbf{L} = \sum_i \mathbf{l}_i$. The same is true for the spins of the electrons form-

ing $\mathbf{S} = \sum_i s_i$. Both vectors precess around the z-axis. In this case the two quantum numbers $\Lambda = |M_L|$, $\Lambda = 0, 1, 2, \dots, L$ and $\Sigma = M_S = s, s-2, \dots, -s$ are introduced as projections of \mathbf{L} and \mathbf{S} respectively. For Hund's case (a) Ω is defined as the sum of Λ and Σ :

$$\Omega = |\Lambda + \Sigma| \quad (2.15)$$

Molecular denotations

The notation of an electronic state of a diatomic molecule is written with the total spin S , and the two projections $\Lambda = |M_L|$ and $\Omega = |\Lambda + \Sigma|$ as

$$X^{2S+1}\Lambda_\Omega \quad (2.16)$$

Note that the capital letter (X) replaced the principal quantum number n known from the atom section. The molecular denotation uses capital letters (A,B,C,...) to notate states reachable from the ground state. States not reachable are denoted with lower case letters (a,b,c,...). The ground state itself is denoted with X.

The transition rules for molecules are:

1. $\Delta\Lambda = 0, \pm 1$
2. $\Delta\Omega = 0, \pm 1$
3. $\Delta S = 0$

CHAPTER 3

Experimental Setup

This chapter describes the experimental setup of the apparatus in Cluster Lab I, used for the RbSr experiments. A throughout discussion of this setup is given in [17]. The setup of the apparatus in Cluster Lab III, used for the gold experiments, is described the chapters 4 and 5.

The apparatus consists of three chambers which are shown in figure 3.1.

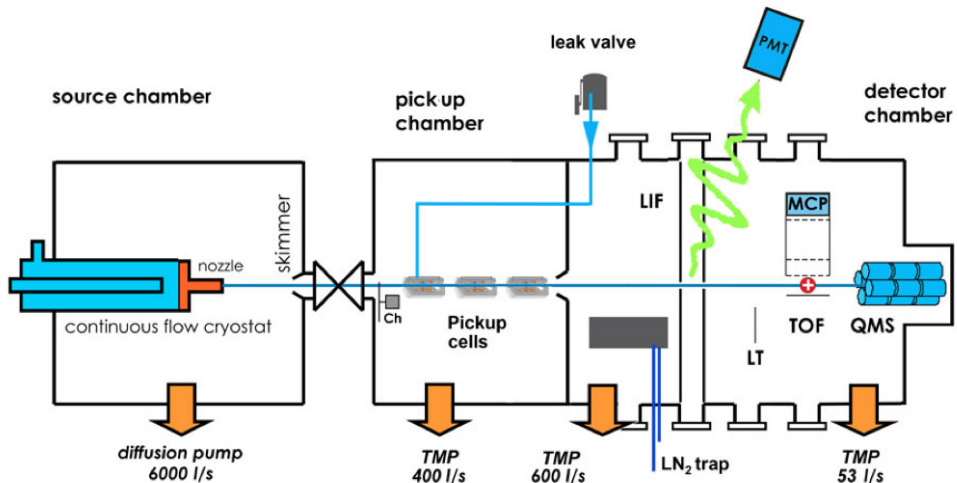


Figure 3.1.: The three main chambers are shown schematically, with measurement devices and pumps. Taken from [34].

The following abbreviations were used in figure 3.1:

TMP ... Turbo molecular pump

Ch ... Chopper

PMT ... Photomultiplier tube

LIF ... Laser induced fluorescence

TOF ... Time-of-flight mass spectrometer

QMS ... Quadrupole mass spectrometer

The blue line, reaching from the nozzle to the end of the detection chamber, represents the helium droplet beam. The beam is created via a supersonic gas expansion through the $5\text{ }\mu\text{m}$ nozzle. A $400\text{ }\mu\text{m}$ skimmer at the end of the source chamber extracts the helium nanodroplets which pick up the dopants in the subsequent pick up chamber. The actual measurements are done in the detection chamber. The apparatus is equipped with many detection devices, prominent for this work are the LIF-spectroscopy setup and the TOF- and QMS mass spectrometer, which are described in detail in section 3.4.

3.1. Source chamber

High purity helium gas (Air Liquide, Alphagaz 2 He B50L L, He $>=99.9999\%$) is used for the preparation of He_N clusters in a supersonic gas expansion. In our experiments the gas is typically forced through the nozzle with a pressure of 60 bar. An oil diffusion pump (Leybold D1 6000 10B) holds the vacuum pressure of the source chamber at 10^{-6} mbar if no helium beam is present and at $\approx 10^{-3}$ mbar if the beam is established [35]. In order to form droplets the gas has to be cooled to temperatures below 25 K. The cooling is done within a heat exchanger built out of two steel pipes fitted into each other (figure 3.2). The gas inlet for the high purity helium is wound around the heat exchanger which is filled with liquid helium from an external dewer (4 K). The cooling has to be maintained during the whole experiment. To ensure constant nozzle temperatures the apparatus is equipped with a Lakeshore 330 Autotuning controller which heats the nozzle when needed. The typical nozzle temperature in our RbSr experiments is 15 K.

3.2. Pick up chamber

The pick up chamber contains different pick up cells to dope the helium droplets with gaseous or solid species. The chopper at the entry of this chamber is important for the alignment process of the nozzle. It is a rotating disk which interrupts the helium beam periodically to distinguish between background and actual helium beam (measured with the QMS). The background is the effusive beam of dopants which reaches the detection chamber even without a helium beam. Figure 3.3 shows the arrangement within the chamber with chopper and the three different pick up cell types.

The first cell is used for doping with gaseous dopants. It is designed as a steel cylinder with an external gas inlet. Because the dopants are already gaseous no heating is required

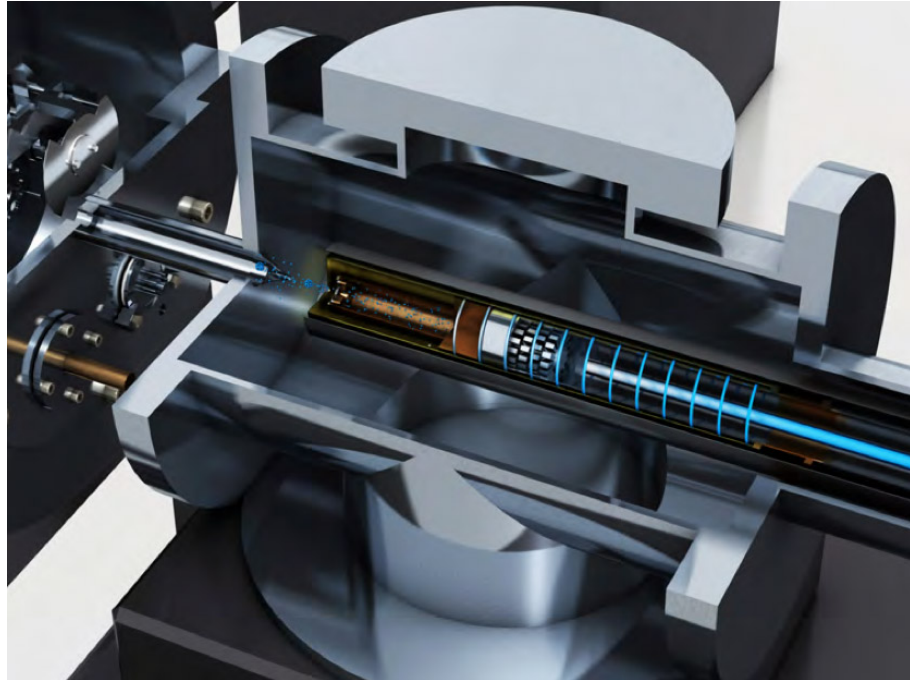


Figure 3.2.: Heat exchanger to cool the high purity helium (spiral wire) and the nozzle to temperatures of about 15 K [35].

in this case. In contrast to this cell type the other two pick up cells in figure 3.3 are able to evaporate solid species. The alkaline metal oven is a steel cylinder with a reservoir for solid species. The cell is connected to an external power supply, controlled by an Eurotherm temperature controller.

The alkaline earth metal oven, designed by Günter Krois, provides several improvements of the steel cylinder type, discussed in detail in [35]. It is made out of copper to react faster to changes of the heating current and to be more efficient. The cell has a temperature shield, which is connected to a thick copper wire transporting heat outside of the apparatus. The shield minimizes the influence on cells nearby which is important because the available room in the pick up chamber is very limited.

A turbo molecular pump holds the vacuum pressure in the chamber at 10^{-6} mbar. Evaporation pressures of about $10^{-3} - 10^{-4}$ mbar are sufficient for the pick up process. In the case of Rubidium and Strontium, cell temperatures of 80 °C and 420 °C are needed to reach those pressures.

After the doping process the droplets enter the detection chamber where the actual experiments are performed.

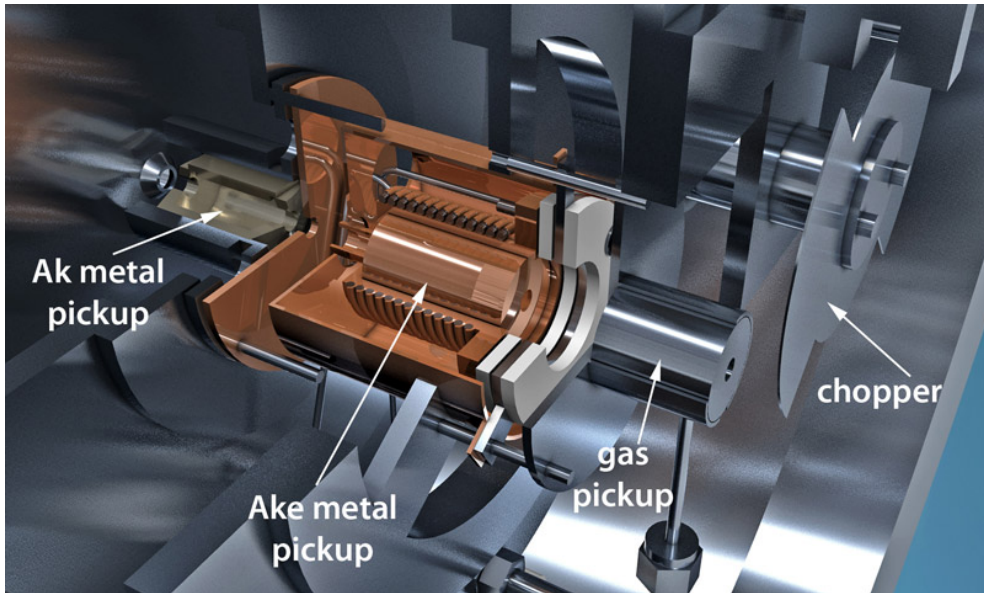


Figure 3.3.: The pick up chamber with chopper and available pick up cell types. Beam enters from the right. Taken from [35].

3.3. Detection chamber

The detection chamber is equipped with the measuring devices and is the last of the three subsequent chambers. A set of pumps hold the vacuum pressure of the chamber in the low range of 10^{-7} mbar. Figure 3.4 shows the arrangement of the LIF spectrometer and the TOF and QMS mass spectrometer.

For LIF spectroscopy the photomultiplier tube (PMT) is used to detect fluorescence light. It is possible to replace the PMT with a grating spectrograph for dispersed fluorescence measurements.

In contrast to that the TOF mass spectrometer extracts ions after laser ionization and measures their different flight times (due to different masses).

The QMS is at the end of the apparatus was mainly used to align the nozzle and therefore the helium beam. A QMS uses an inhomogeneous electrical field, established by four parallel rods, to select ions according to their m/q ratio.

The measuring methods, relevant for this work, are explained in the following.

3.4. Measuring methods

In this section an overview of LIF spectroscopy and REMPI-TOF mass spectroscopy is given. Detailed informations about these methods are found in the referenced literature [36] [2] [34].

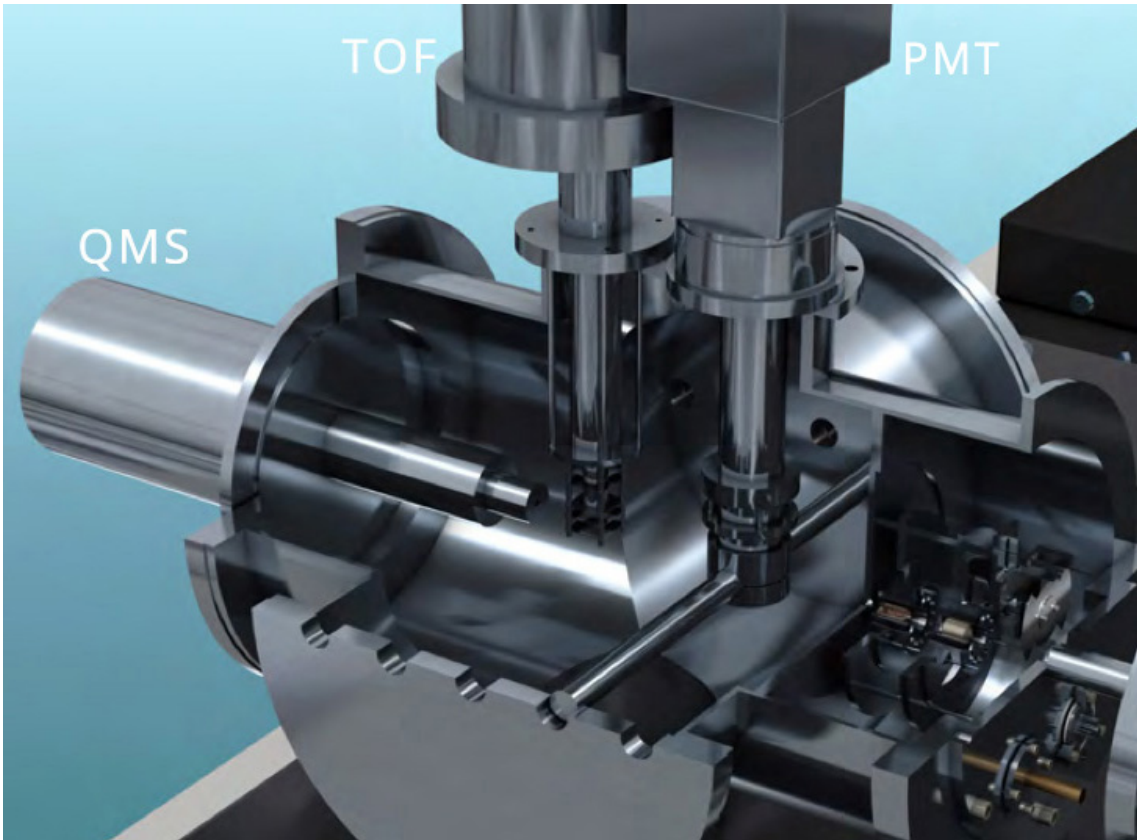


Figure 3.4.: Detection chamber with TOF and QMS mass spectrometer and LIF spectrometer. Modified from [35].

3.4.1. REMPI-TOF spectroscopy

REMPI-TOF spectroscopy (Resonant Multi Photon Ionization) was used to record excitation spectra in the RbSr and Au experiments. Neutral dopants on the helium droplet are ionized by incident laser photons. Ionization is possible either via one- two- or multi photon processes. In a one photon process, a single photon ionizes an atom or molecule directly from the ground state. In a two photon process the first photon excites into a virtual or resonant intermediate state while the second photon ionizes. If the excited intermediate state is a real atomic or molecular state the process is called resonant (Resonant two photon ionization - R2PI). The probability to ionize is much higher via resonant states with high life-times. Ideally the life-time is higher than the pulse duration of the laser.

For the experiments presented in this thesis, the two photon process via a resonant energy level is the most relevant one. In this case the wavelength of a tunable dye laser (Lambda Physik FL 3002) is tuned across resonant energy states. A second laser photon ionizes the atom from the resonant state. Ionization is done either with a fraction of the intensity of the pump laser (Radiant Dyes RD-EXC 200 XeCl laser, 308 nm) or with a second photon of the dye laser. During the ionization process, the dopants desorb from the droplets and are subsequently extracted by the electric field of the TOF. The TOF accelerates the ions

towards a detector where they arrive in different time intervals. Ions per time-intervall are counted. The time of flight is measured from the beginning of each laser pulse. Typically the laser is operated with a frequency of 100 Hz and triggers the counter of the TOF. In case the dye laser excites into a resonant state the ion yield increases, resulting in an excitation spectrum of the dopant in a specific spectral range.

Note that for better resolutions the TOF is operated in reflectron mode. Figure 3.5 shows the TOF set up in reflectron and linear mode.

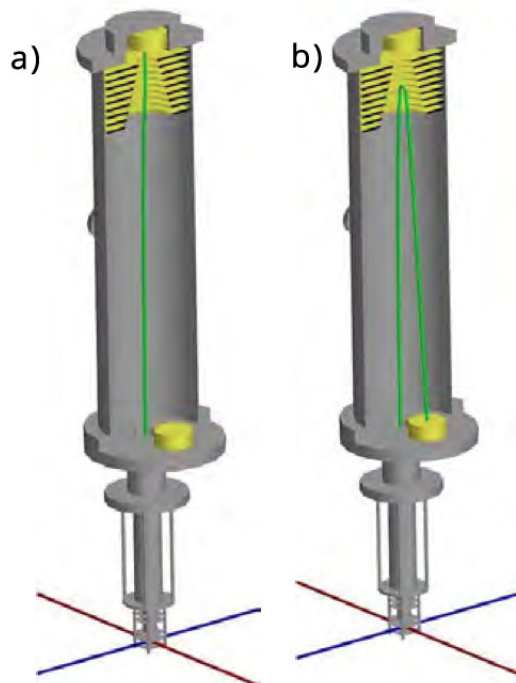


Figure 3.5.: a) TOF in linear mode and b) in reflectron mode. Taken from [35].

3.4.2. Laser induced fluorescence spectroscopy

Laser induced fluorescence is the spontaneous emission of light caused by relaxation of electrons after laser excitation. The emitted fluorescent light is collected by a lens system (shown in figure 3.7) and recorded with a photo multiplier tube (PMT, Hamamatsu R943-01) which is not wavelength dispersive. LIF gives excitation spectra similar to REMPI-TOF spectra, is not mass selective, but more sensitive.

As in REMPI-TOF experiments a dye laser is scanned over resonant states. Figure 3.6 shows different possible relaxations after laser excitation. All emitted photons are amplified to the same degree, but according to the Franck-Condon factors, certain transitions are more likely than others, giving differences in the measured intensities.

To investigate the relaxation process in more detail, dispersed fluorescence is used. For this experiments the PMT is exchanged with a grating spectrograph. Instead of a tunable

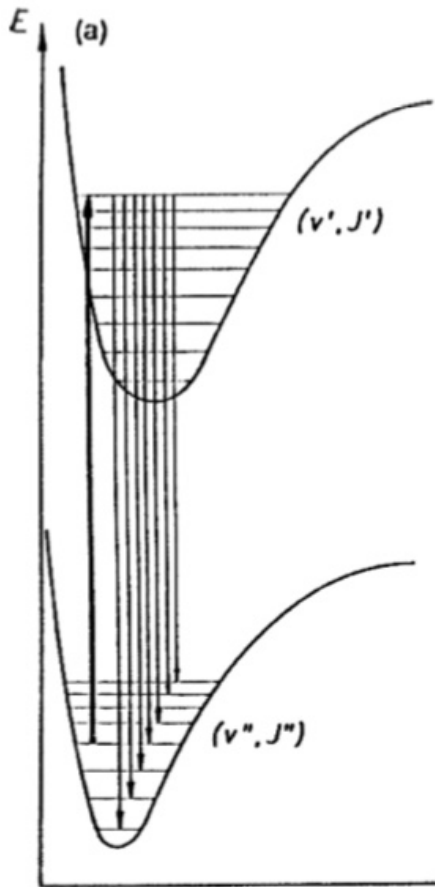


Figure 3.6.: *Indirect relaxation from an excited state into the vibrational ground state.*
Taken from [36].

dye laser a cw ring laser is used for high intensities at a specific wavelength. The cw laser excites exclusively into resonant states. Every relaxation depicted in figure 3.6 causes emission of a photon with a specific wavelength. Those photons are collected by a lens system depicted in figure 3.7 and guided into the grating spectrograph which is scanned over a certain spectral range. A cooled CCD chip (LOT-Andor iDUS DU401ABR-DD) detects the photons and sends the signal to the computer.

Note that a reflector underneath the interaction zone increases the number of photons reaching the detector. To minimize the influence of scattered light the laser is guided within baffle tube.

3. Experimental Setup

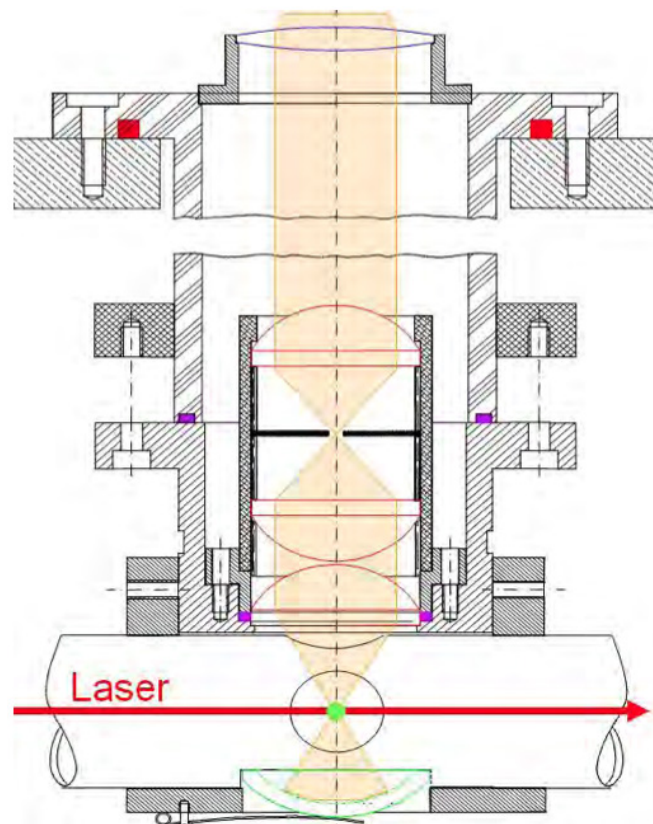


Figure 3.7.: Setup for LIF within the apparatus. Taken from [2].

CHAPTER 4

Experimental Results

This chapter informs about the results of our experiments, carried out during this thesis. The first part of the chapter is dedicated to the RbSr experiments in Cluster Lab I. The second part reports on the results of the gold experiments done in Cluster Lab III. Although different experimental setups were used in the laboratories, this chapter gives REMPI-TOF spectra for RbSr as well as for Gold. Differences in the experimental setup are described in the corresponding section.

4.1. RbSr Experiments

In the course of the PhD Thesis of Günter Krois we investigated the RbSr molecule on the surface of Helium nanodroplets [37]. The spectroscopic results were obtained with REMPI-TOF as well as LIF spectroscopy already explained in chapter 3.4. All experiments regarding the RbSr molecule were executed in Cluster Lab I of the Institute for Experimental Physics in Graz. Chapter 3 describes the experimental setup of this apparatus.

RbSr is an alkali-alkaline earth molecule which is naturally not stable and therefore not observable. In contrast, the helium droplet enables the formation of the molecule on its surface. The two atoms are picked up sequentially by the droplet and their long-reaching van der Waals forces lead to attraction followed by dimerization. The binding energy freed by this process ($\approx 1000 \text{ cm}^{-1}$) causes evaporation of about 207 helium atoms - assuming 5 cm^{-1} binding energy between a helium atom and the droplet. Both atoms have several isotopes which makes mass spectra more complex. The natural isotope distribution of Rb is 72.18%- ^{85}Rb and 27.82%- ^{87}Rb . Sr has three isotopes with an isotopic abundance of 9.86%- ^{86}Sr , 7.0%- ^{87}Sr and ^{88}Sr -82.58%. Therefore a dimer peak in the REMPI spectrum can contain contributions from more than only two specific isotopes. This is shown in

figure 4.1. The green bars illustrate the percentage of Rb atoms whereas the magenta ones show the contribution of Sr atoms. In the dimer diagram, on the right, the blue bars represent the RbSr molecule. The mass spectrum shown in figure 4.1 was taken during the REMPI-TOF recording of the $4^2\Sigma^+ \leftarrow X^2\Sigma^+$ transition.

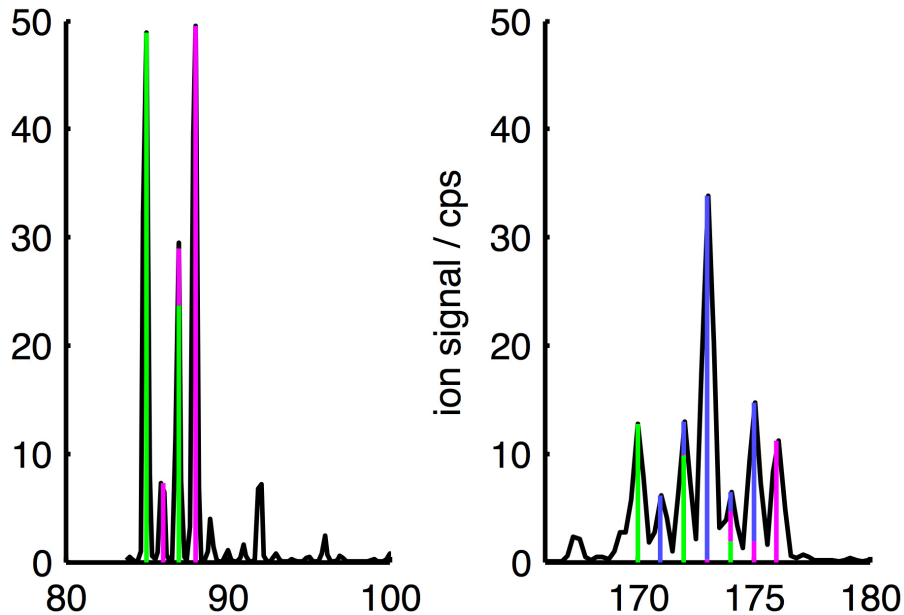


Figure 4.1.: Example of a REMPI-TOF mass spectrum showing Rb and Sr monomers on the left and dimers on the right. The black graph is the ion yield of the TOF-spectrometer. The green and magenta bars show the contribution of the atoms Rb and Sr respectively, whereas the blue bars represent the RbSr molecule.

During the experiments we found an optimum pickup temperature of about 80 °C for Rb and 420 °C for Sr. If not stated otherwise all spectra were recorded at these temperatures. For REMPI-TOF spectra a dye laser (Lambda Physik FL 3002) was used to excite the dopants and a fraction of the pump laser (Radiant Dyes RD-EXC 200 XeCl laser, 308 nm) was used to ionize them. Our results cover a spectral range from 11600 cm^{-1} - 23000 cm^{-1} (overview in figure 4.2). From an energy of 14700 cm^{-1} upwards two photons of the dye laser are sufficient to ionize RbSr. All REMPI-TOF spectra were recorded with the Jordan D-850 AREF TOF with angular reflectron and show ion yield versus dye laser wavelength. The RbSr transition around 14200 cm^{-1} was also investigated with LIF spectroscopy using a photomultiplier tube (Hamamatsu R943-01).

The overview in figure 4.2 shows all six peaks within the available spectral range. The gray graph represents the data points whereas the black line corresponds to the smoothed data. Red and blue are the products of the Franck-Condon factors (FCF) and the squared transition dipole moment (TDM) for the Σ and Π states. In the following this product is referred to as "transition probability". The calculated transition probabilities make it possible to assign peaks to transitions.

The $4^2\Sigma^+ \leftarrow X^2\Sigma^+$ transition is the only vibrationally resolved one and is described in

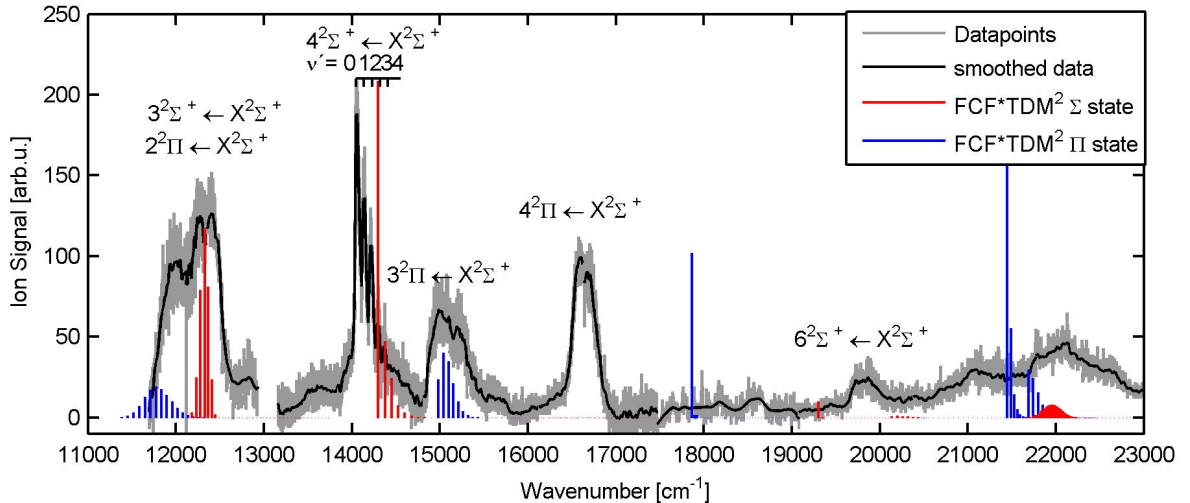


Figure 4.2.: Overview of all six peaks within the available spectral range. The gray graph represents the data points whereas the black line corresponds to the smoothed data. Red and blue are the transition probabilities for the Σ and Π states respectively.

more detail at the end of this section. The other five transitions appear as broad structures which do not allow the identification of individual features. The double peak at 12000 cm^{-1} is in agreement with the theoretical transition probabilities (shown as red and blue bars) suggesting two overlapping transitions. The peak at lower energy is identified as the $2^2\Pi \leftarrow X^2\Sigma^+$ transition. The peak at higher energy corresponds to the $3^2\Sigma^+ \leftarrow X^2\Sigma^+$ transition. Both transitions correlate to the atomic asymptote of the energies of the Rb 5s 2S ground state and the Sr 5s5p 3P excited state.

The structure at 15000 cm^{-1} is assigned to the $3^2\Pi \leftarrow X^2\Sigma^+$ transition. In this energy range an R2PI scheme via ionization with a dye laser photon was applied.

For higher excited states, above 16000 cm^{-1} , figure 4.2 shows, that the results of experiment and theoretical calculations differ. The proximity of Rb and Sr levels and an increasing density of molecular states make theoretical calculations increasingly difficult. In this range calculations can vary around 1000 cm^{-1} . If this is taken into account the theoretical transition at 17900 cm^{-1} ($4^2\Pi \leftarrow X^2\Sigma^+$) can be assigned to the structure at 16800 cm^{-1} .

The same can be applied for the $6^2\Sigma \leftarrow X^2\Sigma^+$ transition. The broad structure at 19800 cm^{-1} can be assigned to the theoretical transition at 19300 cm^{-1} .

This shows, that the $4^2\Pi \leftarrow X^2\Sigma^+$ transition is overestimated by about 1000 cm^{-1} whereas the $6^2\Sigma \leftarrow X^2\Sigma^+$ is underestimated by about 500 cm^{-1} in the theoretical calculations.

Noch Beschreibung der Potentialkurven in figure 4.3 und Zusammenhang mit obiger Beschreibung...

$4^2\Sigma^+ \leftarrow X^2\Sigma^+$ transition

The $4^2\Sigma^+ \leftarrow X^2\Sigma^+$ transition at 14200 cm^{-1} was investigated with TOF and LIF spectroscopy. The resulting spectra are shown in figure 4.4. The figure is divided into three

4. Experimental Results

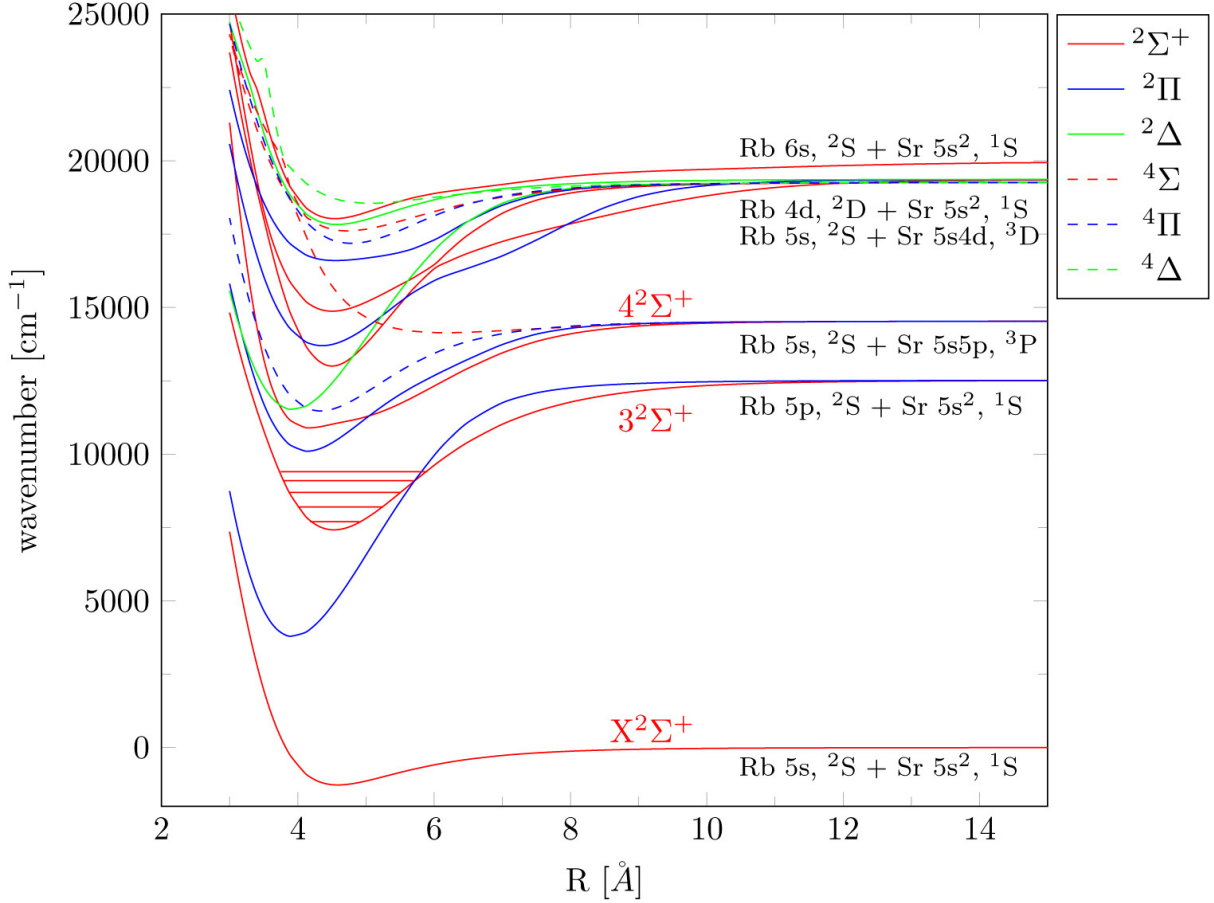


Figure 4.3.: Potential energy curves...

sections a), b) and c). In a) the gray line shows the original REMPI-TOF ion yield. The red graph represents the smoothed data. Green denotes the fitted signal. The signal shows five peaks corresponding to the vibrational transitions $\nu' = 0 - 4 \leftarrow \nu'' = 0$. Due to the low temperature of the system (0.37 K) every excitation starts in the vibrational ground state of the molecule $\nu'' = 0$. The peaks show asymmetric broadening to higher energies, caused by strong interactions with the droplet. This results in a lambda shaped peak form.

Section b) in figure 4.4 shows the LIF spectrum of the vibrational transitions $\nu' = 0 - 4 \leftarrow \nu'' = 0$. In this case the $\nu' = 0 \leftarrow \nu'' = 0$ is much higher than the other four transitions. The signal height fits the calculated transition probabilities, denoted as vertical bars, better in the LIF experiment. But it also shows an underlying background, shifting the spectrum upwards. The reasons for this background can be seen in section c) of figure 4.4. c) shows the molecule $^{85}\text{Rb}^{88}\text{Sr}$ (red), and the single atoms ^{85}Rb (blue) as well as ^{88}Sr . The cyan line represents the REMPI-TOF signal of the $^{88}\text{Sr}^{87}\text{Sr}$ molecule recorded in an experiment optimized for Sr_2 pickup. This signal clearly shows an increase in the range of the background (b), indicating a Sr_2 transition. To minimize the influence of Sr dimers and especially trimers the pick up temperature was lowered, but the background

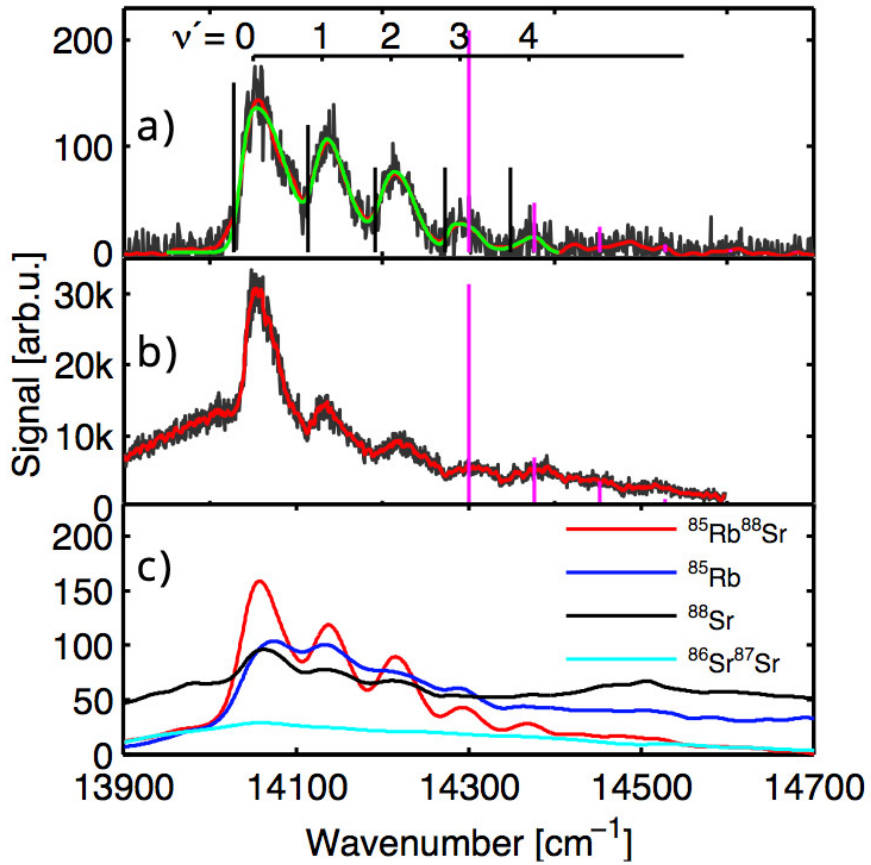


Figure 4.4.: The $4^2\Sigma^+ \leftarrow X^2\Sigma^+$ transition in detail. a) REMPI-TOF spectrum. Gray shows the original ion yield, red the smoothed and green the fitted data. The black vertical line marks the onset of the rising edge of the corresponding free molecule transition. b) Shows the LIF spectrum for the transition. c) A comparison of different REMPI-TOF signals to investigate the cause of the background shown in b). The cyan Sr₂ signal was recorded in a separate experiment.

could not be suppressed entirely during our experiments.

4.2. Au experiments

Gold has always had its place in different technical applications. Electronics, optics or materials science are just a few examples. With the rise of nanotechnology gold got even more interesting, especially in life sciences [38], [39]. Fundamental research in this area can therefore yield to benefits in several scientific fields, not only physics. Despite these promising prospects, spectroscopic data for gold atoms in helium nanodroplets are rare. Moroshkin reported about gold transitions in solid and liquid matrices in the wavelength range below 27500 cm⁻¹ [42]. In contrast, the elements silver and copper, with similar

electronic configurations, have already been investigated [40] [41]. It was part of this thesis to obtain REMPI spectra of gold atoms in helium nanodroplets in the available wavelength range of $37200 - 40000\text{ cm}^{-1}$. The following section reports on the results.

The gold experiments were performed in Cluster Lab III of the institute of experimental physics in Graz. The apparatus in this laboratory is designed to investigate very large clusters of up to 100000 amu. For this reason the apparatus is able to vary the stagnation conditions over a wide range. Temperatures of about 3.8 K (at 20 bar) and helium pressures of 100 bar are possible. The principle setup of the apparatus is very similar to the one used in the RbSr experiments and explained in detail in chapter 3). Therefore only the main differences to the apparatus in Cluster Lab I are listed below:

- The nozzle is cooled with a cold head which can be controlled via PC.
- A high temperature oven, described in chapter 5, was used for the pick up.
- The apparatus is equipped with a TOF spectrometer with angular reflectron (Kasdorf RFT50), a QMS and a micro balance. For the experiments in this section, only the TOF spectrometer was used.

Because the gold experiments were the first spectroscopic investigations in this laboratory, a laser system had yet to be installed. To cover the wavelength range from 37200 cm^{-1} to 40000 cm^{-1} the Indigo-S laser, from Cluster Lab I, was set up. The following provides a short introduction of this laser. Explanations in much more detail can be found in refs [2] [43].

The Indigo-S laser

The Indigo-S is a Ti:sapphire laser pumped by a pulsed Coherent Evolution-15 laser. The pump laser produces pulses with a repetition rate of 5 kHz (200 μs pulse distance, 29 ns pulse duration). The Evolution-15 laser consists of a diode laser pumped Nd:YLF crystal, operated in Q-switch mode. In this mode the diode laser populates the upper laser level of the active medium until population inversion is at its maximum. By then oscillation is prevented through high losses within the resonator. In that way the Evolution-15 provides short laser pulses with high output powers at 532 nm. The pulses of the Evolution laser pump a Ti:sapphire laser with a fundamental wavelength of 750 – 920 nm. During the gold experiments the 193 nm mirror set was used to cover a fundamental wavelength range of 750 – 840 nm. With subsequent crystals the frequency of the fundamental beam can be doubled (375 – 460 nm) and tripled to reach the desired range of 250 – 307 nm. Because the power varies over wavelength it was measured externally with a power-meter. The wavelength was measured with the internal spectrometer of the Indigo-S laser. Attempts to measure it externally with a wavemeter were not successful, because the values changed significantly when only the position of the wavemeter diode was changed.

4.2.1. REMPI spectra

REMPI spectra are obtained by ionizing Au- He_N clusters with the Indigo-S laser and measuring the ion yield of a time-of-flight spectrometer. In case of the investigated Au transitions, a 2 photon ionization scheme can be applied. The involved states are shown in the Gotrian diagram below (figure 4.5). The listed energies correspond to the free atom and were taken from the NIST database [44]. The resonant one photon transition is illustrated with the arrow ν_1 . The curly arrows indicate radiationless relaxations. All energies correlate to the free gold atom. The ionization threshold is at 74718 cm^{-1} . Note that the two D-states are meta stable.

The electron configuration of gold in its ground state is $[\text{Xe}] 4f^{14}5d^{10}6s^1$. As the Gotrian diagram shows 4.5 the resonant transition from the ground state into the first excited state ($5d^{10}6p\ ^2P_{1/2}$) corresponds to an energy of 37359 cm^{-1} . This implies that a second photon, with the same energy, is already sufficient to ionize the atom ($2 \cdot 37359\text{ cm}^{-1} = 74718\text{ cm}^{-1}$).

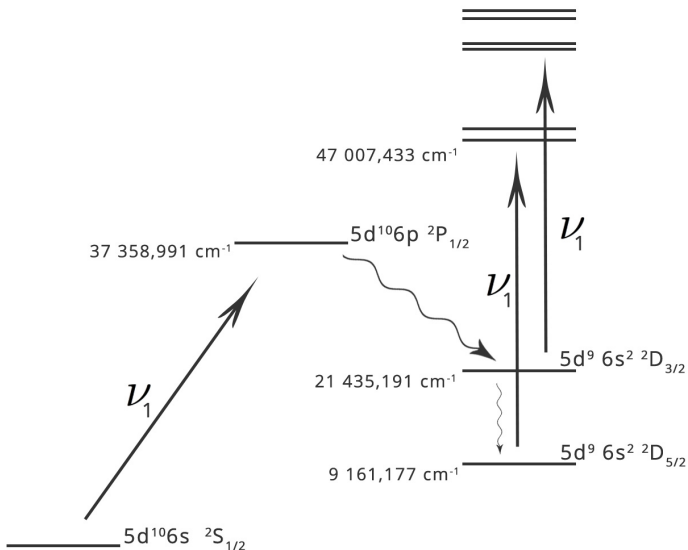


Figure 4.5.: Gotrian diagram with ground state ($5d^{10}6s\ ^2S_{1/2}$) and first excited state $5d^{10}6p\ ^2P_{1/2}$. All energies correlate to the free atom. ν_1 represents the incident laser photon.

When obtaining REMPI spectra the Indigo-S laser has the disadvantage that it can not be continuously tuned. Consequently the spectra are taken at discrete wavenumbers in 2 nm and 0.6 nm steps. The latter corresponds to the minimal wavelength distance between two laser modes, accessible with the HR mirror of the Ti:sapphire resonator. The change from one laser mode to the next is done manually and causes a slight change in the laser path resulting in a displacement ($\approx 0.5\text{ mm}$ at the TOF) which has to be corrected. Although iris diaphragms were used to mark the laser path, the realignment is not perfect which affects the reliability of the recorded spectra. Therefore the recorded spectra differ slightly, which makes the present interpretation speculative. In order to obtain more reliable spectra, the experiment will be repeated to guarantee the reproducibility of the

observed spectral features.

Every excitation measurement at a specific wavelength results in a REMPI spectrum for all masses. To get spectra for a specific mass like Au, AuHe or AuHe₂ all spectra are summed over the desired mass interval. Figure 4.6 shows the first attempt to build a REMPI spectrum out of 27 single measurements (2 nm steps) in the range of 37200–40000 cm⁻¹.

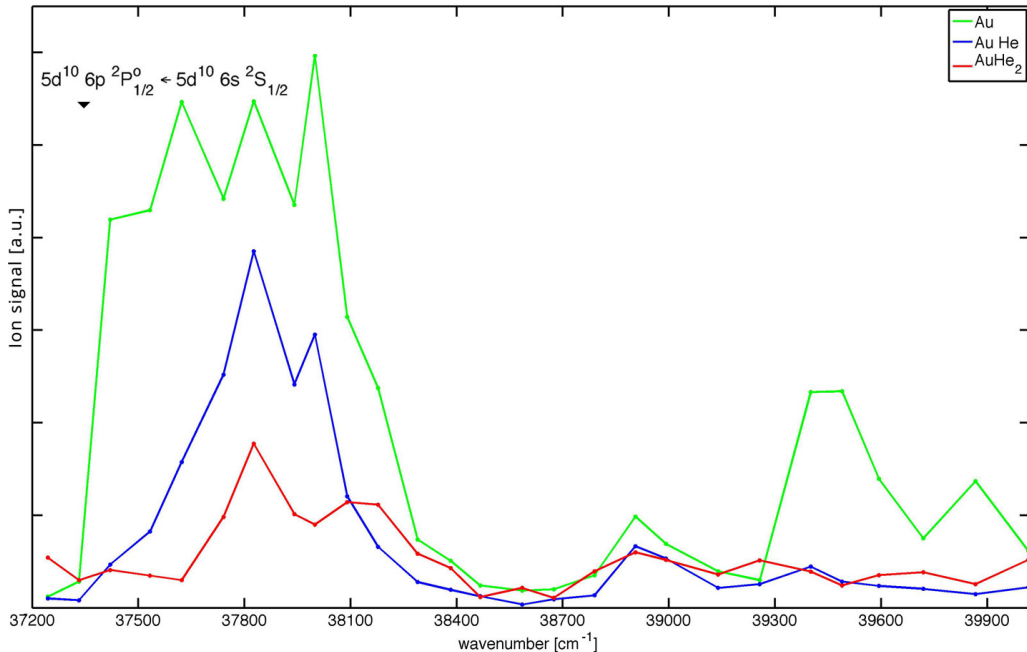


Figure 4.6.: REMPI spectra showing the results for Au (green), AuHe (blue) and AuHe₂ (red). 2 nm steps. The Indigo-S laser was tuned in steps of 2 nm. The transition from the ground state to the first excited state in the free gold atom is marked.

Figure 4.6 shows the first attempt to obtain REMPI spectra for the masses Au, AuHe and AuHe₂. The most prominent feature is a very broad transition (FWHM ≈ 790 cm⁻¹) between 37350 cm⁻¹ and 38400 cm⁻¹. The width suggests that the transition occurs in the droplet. The rising edge of this broad transition fits the position of the $5d^{10}6p^2P_{1/2}^o \leftarrow 5d^{10}6s^2S_{1/2}$ free atom transition well. To be more specific a second spectrum, with smaller wavelength distances of about 0.6 nm, was recorded. This is the minimal step size of the Indigo-S without changing the position of the HR mirror and the Etalon.

Figure 4.7 shows the Au spectrum in 2 nm steps in comparison to Au, AuHe and AuHe₂ in 0.6 nm steps denoted with "fine". Whereas the first attempt only showed a broad, featureless structure, the Au signal (magenta) now shows identifiable features. The peak at 37300 cm⁻¹ can be assigned to the $5d^{10}6p^2P_{1/2}^o \leftarrow 5d^{10}6s^2S_{1/2}$ free atom transition. The steep rising edge indicates an atomic transition and is characteristically blue shifted. The sharp atomic lines originate from atoms being rejected from the helium droplet after excitation. There are two transitions very similar in energies, $5d^{10}6p^2P_{1/2}^o \leftarrow 5d^{10}6s^2S_{1/2}$ and

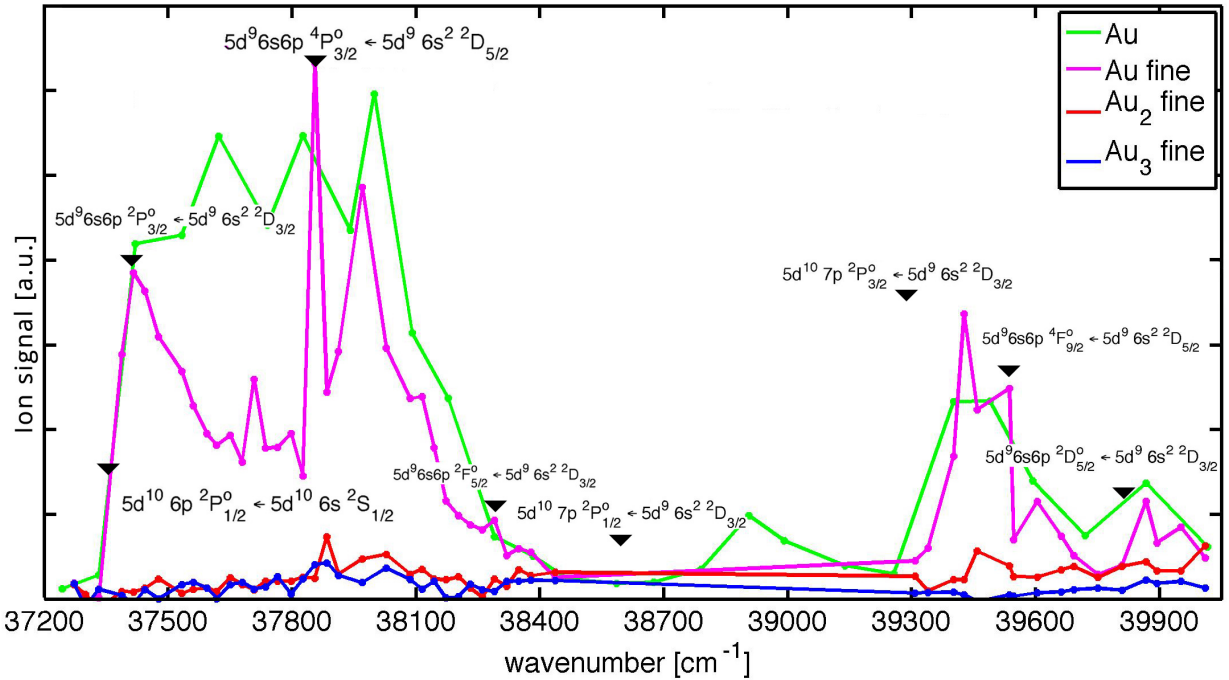


Figure 4.7.: The spectrum compares the results obtained in 2 nm and 0.6 nm steps for Au (green and magenta). The spectra in 0.6 nm steps are denoted as "fine". Au dimer (Au_2) and trimer (Au_3) are depicted in red and blue, respectively. The energies of possible transitions in this wavelength range are marked.

$5d^96s6p^4P_{1/2}^o \leftarrow 5d^96s^2\ ^2D_{5/2}$. Therefore it can be assumed that the peak at 37350 cm^{-1} contains contributions of both transitions. Note, that because no theoretical data is available all peaks were assigned via comparing the free atom energies from the NIST database with the obtained spectra.

The second feature revealed in the Au spectrum is the sharp line at 37840 cm^{-1} . This peak can be assigned to the $5d^96s6p\ ^4P_{3/2}^o \leftarrow 5d^96s^2\ ^2D_{5/2}$ transition. The $^2D_{5/2}$ state is reached via radiationless relaxation, which is enabled by the helium droplet. Both D-states are meta stable with life times high enough for a second excitation by a laser photon. Consequently for those transitions a three photon ionization scheme can be applied.

In summary, within the wavelength range of the Indigo-S, there are eight possible transitions. One excitation directly from the ground state and seven from the two D-states. Two of those seven excitations start from the $5d^96s^2\ ^2D_{5/2}$ state and five from the $5d^96s^2\ ^2D_{3/2}$ state. Table 4.1 gives an overview of the excitations with involve the two D-states.

Comparison with Cu and Ag

As mentioned in the introduction of this chapter, spectroscopic data for the atoms Cu and

4. Experimental Results

Table 4.1.: Possible transitions within the spectral range of the Indigo-S (32000 – 40000 cm⁻¹) for the free atom with respective wavenumbers. From the subtraction in the right column the energies of upper and lower state can be obtained [44].

Denotation of possible transitions from the D-states	energy difference [cm ⁻¹]
$5d^9 6s6p \ ^4P_{3/2}^o \leftarrow 5d^9 6s^2 \ ^2D_{5/2}$	47007, 433 – 9161, 177 = 37846, 256
$5d^9 6s6p \ ^4F_{9/2}^o \leftarrow 5d^9 6s^2 \ ^2D_{5/2}$	48697, 147 – 9161, 177 = 39535, 97
$5d^9 6s6p \ ^2P_{3/2}^o \leftarrow 5d^9 6s^2 \ ^2D_{3/2}$	58845, 414 – 21435, 191 = 37410, 223
$5d^9 6s6p \ ^2F_{5/2}^o \leftarrow 5d^9 6s^2 \ ^2D_{3/2}$	59713, 2 – 21435, 191 = 38278, 009
$5d^{10} 7p \ ^2P_{1/2}^o \leftarrow 5d^9 6s^2 \ ^2D_{3/2}$	60032, 85 – 21435, 191 = 38597, 659
$5d^{10} 7p \ ^2P_{3/2}^o \leftarrow 5d^9 6s^2 \ ^2D_{3/2}$	60728, 49 – 21435, 191 = 39293, 299
$5d^9 6s6p \ ^2D_{5/2}^o \leftarrow 5d^9 6s^2 \ ^2D_{3/2}$	61255, 1 – 21435, 191 = 39819, 909

Ag with similar electronic configurations are already available. The elements are within the same group of the periodic table and therefore a comparison of the available spectra is very interesting. Figure 4.8 shows the comparison of Cu, Ag and Au. The wavelength axis was scaled proportional. Note, that the Au and Ag spectra were recorded with REMPI-TOF whereas the Cu spectrum was obtained with a quadrupole mass spectrometer.

In all three spectra the $^2P_{1/2} \leftarrow ^2S_{1/2}$ transition, marked with a gray line, can be observed. Cu and Ag both show the two atomic transitions $^2P_{1/2} \leftarrow ^2S_{1/2}$ and $^2P_{3/2} \leftarrow ^2S_{1/2}$. The fine structure splitting of the 2P level depends on the spin-orbit interactions which is proportional to the atomic number. Therefore the $^2P_{3/2}$ state is not observable for gold within the available wavelength range of the Indigo-S laser. Even for Ag the fine structure splitting of the level is with 950 cm⁻¹ big, compared to Cu with 200 cm⁻¹.

The Au spectrum only shares the $^2P_{1/2}$ with the two other spectra. There is a big difference regarding the shape of the peaks. The transitions in the Cu and Au spectra show sharp rising edges directly followed by phonon wings whereas Ag shows zero phonon lines with separated phonon wings. The width of the $^2P_{1/2}$ transition is about 150 cm⁻¹ for Cu whereas it is about 200 cm⁻¹ for Au.

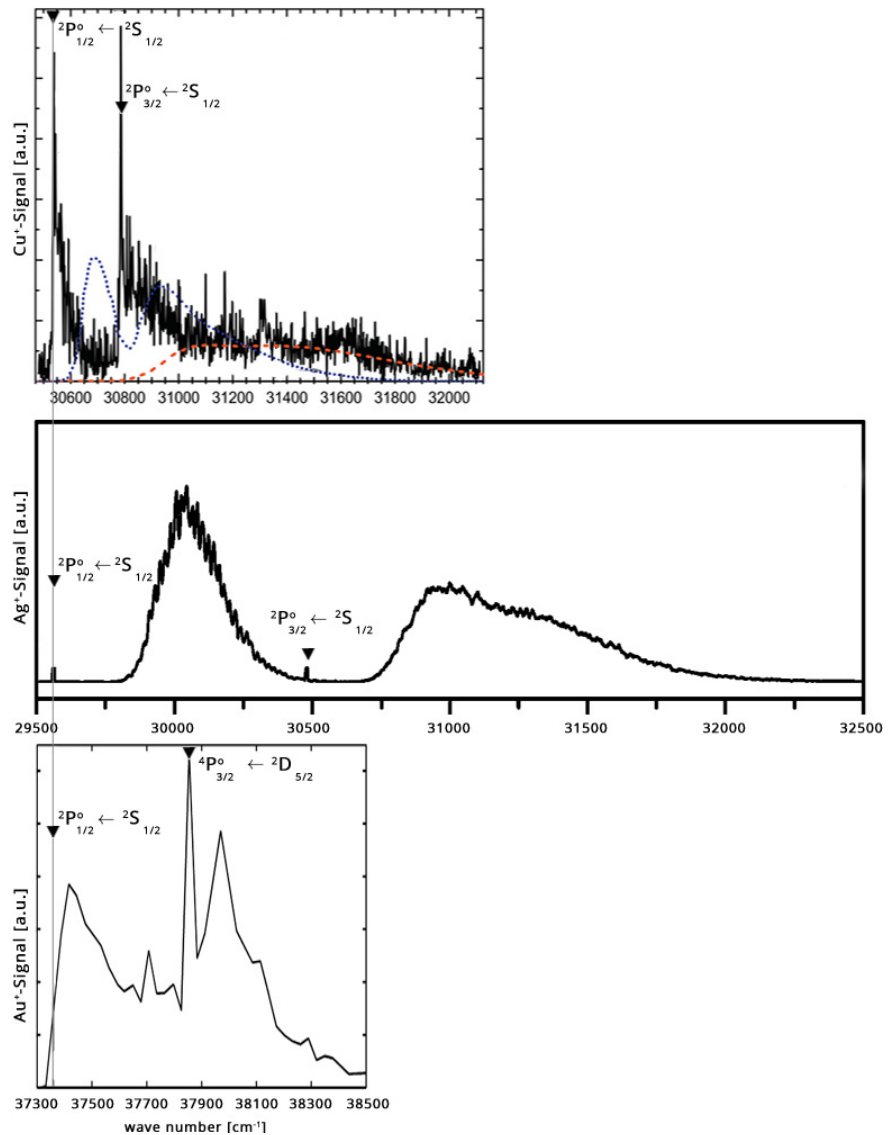


Figure 4.8.: Comparison of the three spectra for a) Copper [41], b) Silver [40] and c) Gold. The gray line marks the $^2P_{1/2} \leftarrow ^2S_{1/2}$ transition observable for all three elements. The spectra for Au and Ag are REMPI spectra whereas Cu was obtained with a QMS.

CHAPTER 5

High temperature pick up source for gold

This chapter describes the pick up source which was designed for high temperature metals and was used in the course of this thesis as a pick up oven for Gold (Au). The main issues were the construction and implementation of the oven into the apparatus in Cluster Lab III as well as considerations for a direct temperature measurement of the liquefied metal. In addition a temperature controller was programmed in LabView which is described in detail in chapter 6.

Temperatures higher than 1064 °C are needed in order to produce vapor pressures high enough for doping He_N clusters with Au atoms. An aluminum coated tungsten wire basket (Ted Pella, basket style 6 [45]) is used to evaporate the material. This basket allows to reach a maximum temperature of 1800 °C. According to the data sheet the temperature, which can be applied over unlimited time periods, is limited to 1475 °C. The maximum heating current is 49 A with an overall heating power of 768 W. Detailed informations about the basket can be found at [45].

5.1. The oven setup

The new oven design fits in all pick up chambers of our cluster laboratories at the institute of experimental physics in Graz. It was designed by Phillip Thaler and fulfills some important requirements:

- The oven has a water cooled shield to minimize the influence of other ovens nearby.

5. High temperature pick up source for gold

- The modular design allows extending the pick up source with a second basket.
- It provides adaptable current connectors on the bottom side of the base plate.

All gold experiments were done with the two basket setup, shown in figure 5.2, whereas silver experiments were performed with only one basket. In case of two baskets the second one is mounted flipped above the first one. The inner surfaces of the baskets face each other in this setup. Both baskets are then heated with the same current. In this way the second basket minimizes losses and confines the gold vapor pressure within the volume of the two baskets. This is especially important for an expensive material like gold. Figure 5.1 shows one basket with gold.

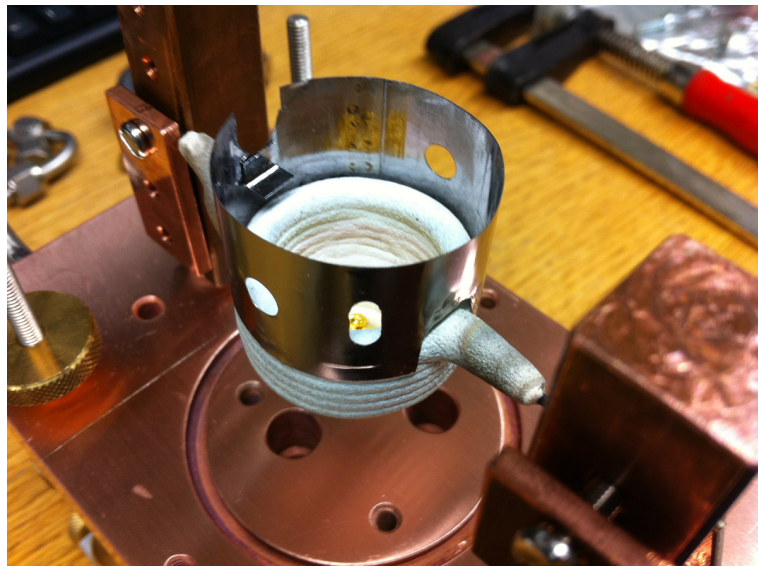


Figure 5.1.: *Pick up source with the first basket filled with gold. The second oven is mounted flipped above the first one. The molybdenum ring provides an additional confinement for the gaseous metal. The whole setup is surrounded by a cooling shield in the final setup.*

The two centered circular holes in the molybdenum ring are the entry and exit holes for the helium droplet beam. The remaining third long hole is the lead through for the thermocouple. The fully assembled oven is shown in figure 5.3.

When assembling the oven one has to make sure that the entry and exit holes of the cooling shield, as well as those from the molybdenum ring are aligned properly. For this purpose a small brass pipe with the diameter of the entry and exit holes was used. It turned out that this pipe is also a great help to keep everything in place while the gold source is installed in the pick up chamber of the apparatus. The problems and best practices during the assembly are described in the following section.

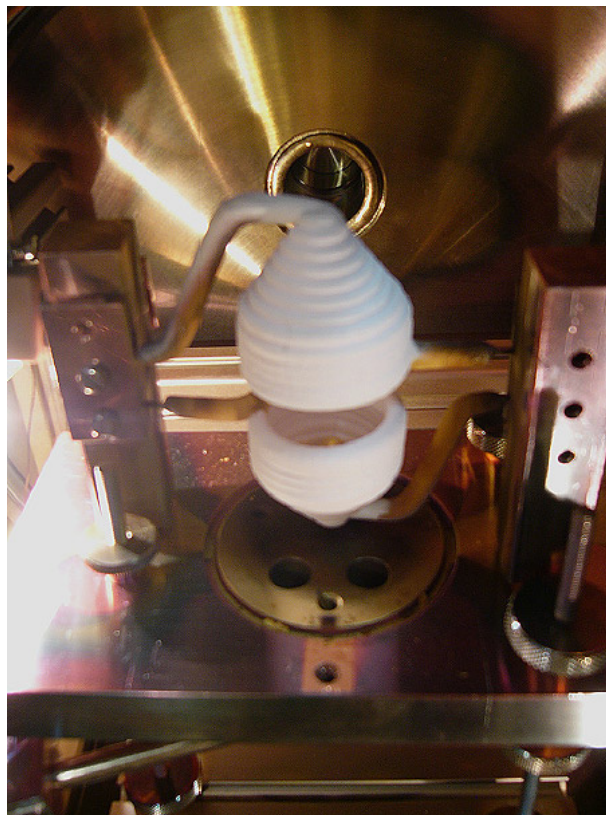


Figure 5.2.: Two-basket setup in the pick up chamber of the apparatus in Cluster Lab III. For illustration purposes without Molybdenum ring.

5.2. Temperature measurements

Temperature measurements can quickly become complicated when measuring high temperatures of liquefied materials. In the past, conventional methods to determine the temperature of the dopant were based on temperature measurements of the pick up cell. Not the liquid itself. In addition those methods did not offer the possibility to log and control the temperature via a computer. Both problems were solved during this thesis.

5.2.1. Mounting the thermocouple

To measure the temperature with a thermocouple one has to make sure, that the only connection of the two thermocouple wires is at the point where the temperature should be measured. This means, that the wires have to be protected from the vapor pressure within the pick up source. Evaporated metal condenses on the thermocouple wires and causes short-circuits. As a consequence the temperature is measured at the point where the two thermocouple wires are connected through the condensed metal. For our experiments the problem was solved with a ceramic tube (3 mm diameter) with only one open end. This tube dips with the closed end into the liquid metal, shielding the thermocouple



Figure 5.3.: Fully assembled gold oven with cooling shield and thermocouple. The connectors for the water cooling are made of high quality steel for durability. The brass pipe to align entrance and exit holes is still in place.

inside the tube, from the liquid and the vapor pressure on the outside of the tube. It is essential that the tube protects the thermocouple wires until they reach the feed through of the water cooled copper shield (figure 5.3).

To make sure, that the wires inside the tube are not connected, a separator was made out of a conventional isolation element shown in figure 5.3. The isolation element was grinded until it was small enough to fit into the ceramic tube (together with the thermocouple).

The high temperatures in our gold experiments make it necessary to use type C thermocouples instead of type K. Temperatures of up to 2000 °C can be measured with this type. More informations about type C thermocouples can be found in the data sheet which is available at ref. [46].

5.2.2. Connecting the thermocouple with a Computer

Once the thermocouple is in place and the oven is installed in the pick up chamber, one can connect the thermocouple wires with the feed through on the inside of the pick up chamber. The outside of the feed through is connected directly with the Voltcraft Datalogger K204 which is used to measure the thermo voltage. The data sheet for the Datalogger can be found at ref. [47].

Although the Datalogger is connectable with a computer, it is not recommended to do this directly. The temperature measurements are known to be unreliable in this case. To prevent this, the Datalogger is connected with an optocoupler which sends the data to the

computer. The reason for the unreliable measurements are most likely unwanted ground connections between the ports of the Datalogger.

The next step is to connect computer and power supply to control the heating current and therefore the temperature.

5.2.3. Connecting the power supply

The power supply (Elektroautomatik PS9000), used to supply the heating current for the oven, offers a parallel port for remote control. The manufacturer provides a sample LabView program to communicate with the device. To connect computer and power supply, a parallel-USB adapter, also available from Elektroautomatik, is needed (UTA12 interface ref. [48]). While the UTA12 is directly connected with the computer via USB, a customized parallel cable is used to connect the UTA12 with the parallel port of the power supply. A data sheet with the pin assignments of this cable is available on the website of Elektroautomatik [48]. The pin assignment, which actually works, is not identical with the one listed in the data sheet. The working pin assignment developed during a trial and error process and is listed in table 5.1. Figure 5.4 shows the connectors schematically to define the pin numbers. The connectors are drawn from the back side. The parallel connector is male, the serial is a female.

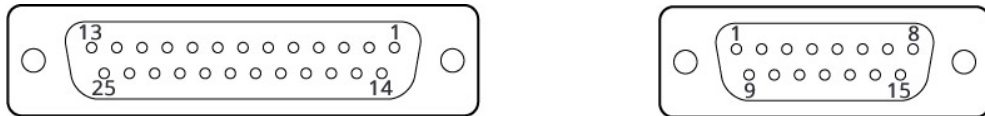


Figure 5.4.: Parallel (left) and serial (right) connectors viewed from the back side.

Table 5.1.: Adapter to connect the serial port from UTA12 with the parallel port of the power supply. "P" specifies the pin number of the parallel port, "S" the number on the serial port.

From Pin number → to Pin number		
1P → 18P	11P → 13S	21P → 23P
2P → 2S	12P → 15S	22P → 5S
3P → 1S	13P → 7S	23P → 21P
4P EMPTY	14P EMPTY	24P EMPTY
5P → 9S	15P → 4S	25P EMPTY
6P → 10S	16P EMPTY	20P → 11S
7P EMPTY	17P EMPTY	10P → 8S
8P → 14S	18P → 1P	19P EMPTY
9P → 6S		

CHAPTER 6

Programming a temperature controller in LabView

This chapter describes the LabView program which controls the heating current of the oven. In previous experiments the oven temperature was controlled by an external PID temperature controller (Eurotherm). Although this setup is well tested, the temperature can not be logged via PC. The Lab View block diagram is documented in the following.

6.1. Requirements

Our first approach to control the temperature of the basket was setting a specific current (at constant voltage). It turned out, that temperatures, set only through a constant current, are not reproducible. Every time the basket is heated up, the same pairs of current and voltage resulted in different temperatures.

Figure 6.1 shows a test, where the basket was heated up to more than 1100°C , held constant at the corresponding voltage/current pair for about 5 minutes and cooled down to 800°C . Note that the graph in figure 6.1 was obtained with a type K thermocouple and empty basket. The results are also quantitatively valid for type C thermocouples.

The figure illustrates both, positive and negative properties of this method. The basket temperature responds linearly to the power which is good. One of the biggest problems can be seen at the maximum temperature. At that point current and voltage were held constant for about 5 minutes, but this didn't result in a constant temperature. The temperature sunk about 30°C without changing current or voltage. During experiments this behavior is unacceptable. The attempt to reach a specific point on the heating curve via cool down also failed. The resulting temperature was about 30°C lower than during the previous heating phase.

Therefore, temperature controlling via setting the heating power, is not sufficient. In

fact we figured out that it is much better to measure the actual basket temperature and hold it constant through regulating the heating current (at constant voltages). A simple controller which heats when the temperature is lower than the desired temperature and switches the power supply off when the temperature is too high gives relatively high jitter ($\pm 40^\circ\text{C}$). Tests showed, that reproducible results with low jitter are only possible with a PID controller (Proportional-Integral-Derivative controller). A PID controller calculates an error value as the difference between the measured temperature and the desired temperature. The error value is minimized by adjusting the heating current.

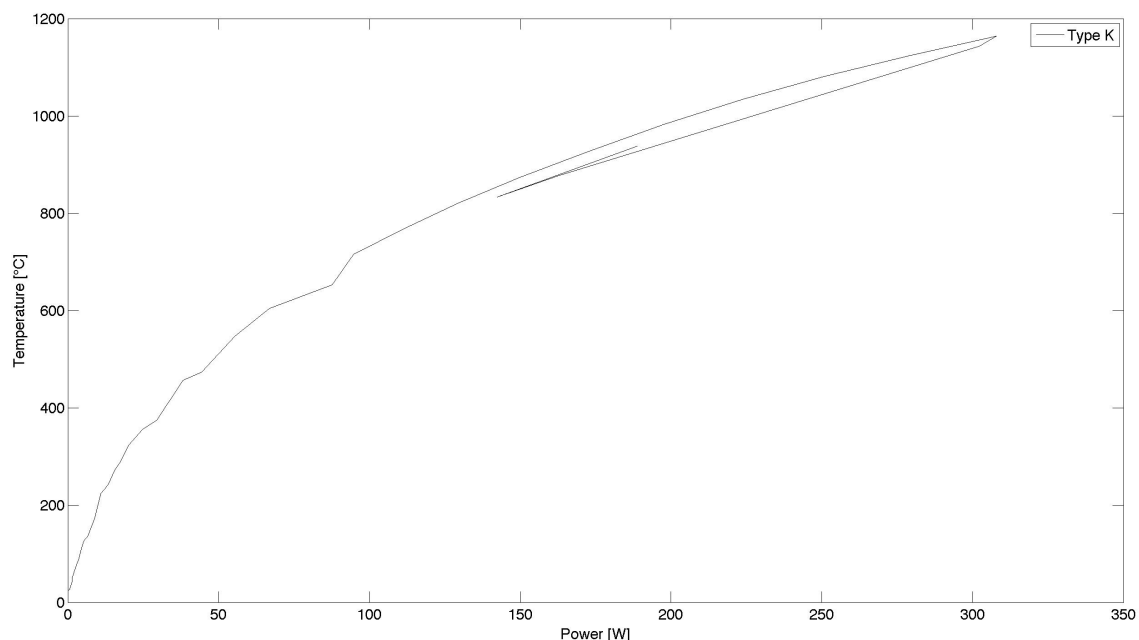


Figure 6.1.: Problems during basket heating tests. The graph shows heating up and holding current and voltage constant at maximum (1150°C). Then cooling down to about 800°C and heating up to 900°C .

After these tests, the required features of the LabView program were defined as follows:

- The program should control the current of an external power supply. The voltage is not preset, it obeys ohm's law.
- The measured temperature should be displayed. Because a conventional Voltcraft Datalogger K204 is used, which natively only supports type K thermocouples, the LabView program has to recalculate the temperature for type C accordingly.
- A software PID controller (provided by the LabView program package) should regulate the heating current, appropriate PID parameters have to be found.
- The basket must not undergo fast temperature changes at temperatures lower than

300 °C. The LabView program should be able to warm up the basket with a temperature gradient lower than 4 °C per minute. The same applies to the cool down process.

- The program should be able to handle one- and two-basket setups.

The LabView block diagram of the final program is documented in the following.

6.2. Documentation of the LabView block diagram

The LabView program is divided into three main parts identifiable through the three sequences (0, 1, 2) of the stacked sequence structure (film strip) in figure 6.2. Sequence 0 scans available power supplies and lists them in a drop down menu. Sequence 1 is responsible for establishing a communication to the power supply and for the calculation of temperatures and currents. Sequence 2 closes the connection to the power supply. No changes were made in Sequences 0 and 2. For more informations relating to this parts have a look at the data sheet provided by the Elektroautomatik [49]. Further explanations in this section only refer to sequence 1.

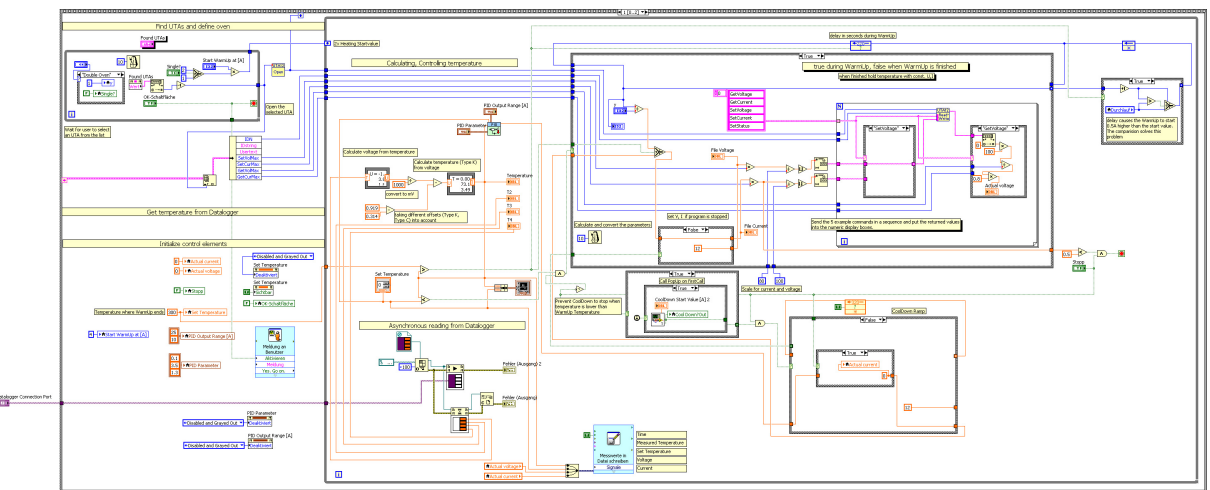


Figure 6.2.: Block diagram of the final LabView program. The stacked sequence structure (film strip) is the outermost frame.

All important parts of the program are labeled with yellow description tags for documentation. The parts "Find UTAs" and the for-loop in the big, outermost case-structure are from the original power supply communication program. The rest was added to establish the required additional functions listed in section 6.1. The following sub sections correspond to the yellow description tags in the block diagram, figure 6.2.

6.2.1. Initialize control elements

The first task of the program is, to initialize control elements and variables. This is done immediately after the program is started, because otherwise it would be possible to start with high heating currents, still preset from previous experiments. The PID parameters ($P = 0.1$, $I = 0.01$, $D = 0.3$) and output range are set as well as the warm up temperature. An exception is the start current for the warm up. Due to the communication with the power supply the current has to be set within the while case, labeled as "Find UTAs and define oven".

When the program has successfully started the user can adjust the setting for starting current, oven type, used power supply and communication port for the Datalogger in the front panel, shown in figure 6.3.

6.2.2. Asynchronous reading from the Datalogger

The section "Asynchronous reading from Datalogger" in the block diagram is responsible for reading the temperature from the Datalogger. The block loads an external vi (saved as "K204 Display.vi") which establishes the connection. The basic functionality of this vi was programmed by Friedrich Lindebner. Tests showed, that it is necessary to integrate this vi asynchronously, because otherwise temperature values are not read. In this case the LabView temperature controller gets "NAN" instead of a real temperature value. The reason for this failure is most likely the different reading cycles of power supply and Datalogger. A good explanation of asynchronous reading in LabView can be found in the LabView help section under "Asynchronously Calling VIs".

6.2.3. Converting the thermal voltage

Once the type K temperature is available in the program, it can be converted into the equivalent type C temperature. This is done in two steps. First of all, the type K temperature is transformed into the corresponding type K thermal voltage using the direct polynomials from the thermocouple manufacturer Omega [50]. For converting type K temperatures above 0 °C the direct polynomial is

$$\sum_{i=0}^n c_i \cdot (t_{90})^i + \alpha_0 \cdot \exp(\alpha_1 \cdot (t_{90} - 126.9686)^2) \quad (6.1)$$

All coefficients $c_0 \dots c_9$ as well as both constants α_0 and α_1 are listed on the Omega website [50].

In LabView the formula is implemented as

$$\begin{aligned}
 U = & -1.7600413686 \cdot 10 + 1.185976 \cdot 10^2 \cdot \exp(-1.183432 \cdot 10^{-4} \cdot (T - 126.9686)^2) + \\
 & 3.8921204975 \cdot 10 \cdot T + 1.185976 \cdot 10^2 \cdot \exp(-1.183432 \cdot 10^{-4} \cdot (T - 126.9686)^2) + \\
 & 1.8558770032 \cdot 10^{-2} \cdot T^2 + 1.185976 \cdot 10^2 \cdot \exp(-1.183432 \cdot 10^{-4} \cdot (T - 126.9686)^2) - \\
 & 9.9457592874 \cdot 10^{-5} \cdot T^3 + 1.185976 \cdot 10^2 \cdot \exp(-1.183432 \cdot 10^{-4} \cdot (T - 126.9686)^2) + \\
 & 3.1840945719 \cdot 10^{-7} \cdot T^4 + 1.185976 \cdot 10^2 \cdot \exp(-1.183432 \cdot 10^{-4} \cdot (T - 126.9686)^2) - \\
 & 5.6072844889 \cdot 10^{-10} \cdot T^5 + 1.185976 \cdot 10^2 \cdot \exp(-1.183432 \cdot 10^{-4} \cdot (T - 126.9686)^2) + \\
 & 5.6075059059 \cdot 10^{-13} \cdot T^6 + 1.185976 \cdot 10^2 \cdot \exp(-1.183432 \cdot 10^{-4} \cdot (T - 126.9686)^2) - \\
 & 3.2020720003 \cdot 10^{-16} \cdot T^7 + 1.185976 \cdot 10^2 \cdot \exp(-1.183432 \cdot 10^{-4} \cdot (T - 126.9686)^2) + \\
 & 9.7151147152 \cdot 10^{-20} \cdot T^8 + 1.185976 \cdot 10^2 \cdot \exp(-1.183432 \cdot 10^{-4} \cdot (T - 126.9686)^2) - \\
 & 1.2104721275 \cdot 10^{-23} \cdot T^9 + 1.185976 \cdot 10^2 \cdot \exp(-1.183432 \cdot 10^{-4} \cdot (T - 126.9686)^2)
 \end{aligned} \tag{6.2}$$

After obtaining the corresponding voltage, one has to take the offset between type K and type C measurements into account. This offset results from the fact, that type K and type C supply different voltages at room temperature (23°C). Voltages and their respective temperatures of type C and type K thermocouples can be obtained from the Omega reference tables [46], [51]. According to these tables the type C supplies 0.314 mV whereas the type K supplies 0.919 mV at room temperature. This offset is subtracted in the LabView block diagram.

For the second step, the transformation of the type K voltage into type C temperature, one needs the recursive polynomial. Unfortunately the data sheet (ref. [50]) does not list polynomials for type C thermocouples. Therefore the polynomial was obtained by manually fitting the type C thermocouple characteristic from the reference table in [46]. For the LabView calculation the following polynomial was used (obtained from the fit):

$$\begin{aligned}
 T = & 0.00036607033979 + 73.15121202 \cdot U - 3.4901476382 \cdot U^2 + 0.2973265406 \cdot U^3 - \\
 & 0.014640523567 \cdot U^4 + 0.00039799817557 \cdot U^5 - 0.0000043837094235 \cdot U^6
 \end{aligned} \tag{6.3}$$

After these calculations the Datalogger temperature for a type K thermocouple is transformed into the respective type C temperature. The results are in very good agreement with type C measurements of an Eurotherm temperature controller.

6.2.4. PID temperature controlling

The PID controller is a ready-to-run vi from the LabView PID Toolkit. For this program the "PID Autotuning (Temperature)" controller was used. Detailed informations about this vi can be found in the LabView documentation under "PID Autotuning (Temperature) VI".

In this implementation only three inputs are used:

- The temperature input. This input supplies the measured and recalculated type C temperature value.
- PID output range. This enables the user to set minimum and maximum heating current.
- The P-I-D parameter input fields to manually enter the P, I and D parameters of the controller.

The P, I and D parameters as well as the PID output range can be adjusted via the front panel (figure 6.3). The PID parameters depend on the temperature and were determined empirically. Good start values are $P = 0.1$, $I = 0.01$ and $D = 0.3$.

The minimum and maximum current values were also determined during tests. With 35 A one can heat up a the single-basket setup to 1100 °C.

The only output of the PID controller is the heating current which is directly sent to the power supply.

6.2.5. Warm up and conventional operation mode

Basically there are three different cases in which the program behaves differently. The warm up phase, the conventional operation mode and the cool down. The first two cases correspond directly to the big case-structure within the while loop (figure 6.2). The true case handles the warm up phase and the false case contains the functionality for normal operation mode. In this two true/false cases most of the functionality is related to the communication with the power supply. Every block is labeled according to its function (for example "Get Current", "Set Current",...).

The warm up mode has to increase the heating current slowly to prevent damage of the basket due to thermal strain. The current is increased in 0.5 A steps in single oven mode and in 1 A steps in double oven mode. By default the time delay between two steps is set to 250 seconds. In LabView this task is done by using a shift register with a callback value. The callback value corresponds to the next current value being set. The logic checks if the actual temperature of the basket is lower than the warm up temperature set at program start. The default warmp up temperature is 300 °C and can be changed manually in the block diagram (section "Initialize control elements"). If the actual temperature is lower

than the warm up temperature the program enters the true case and increases the current via the shift register subsequently every 250 seconds. It stops the warm up when the temperature gets higher than the warm up temperature. Then the false case comes into play. This case is independent from the shift register. It does not heat the basket with the callback value. Instead it heats it with the current determined by the PID controller. Note that the front panel control element "Set Temperature" is not set active during warm up. This control element is deactivated when initialized, to prevent the user presetting any temperatures during warm up.

The callback value for the warm up process has to pass a true/false case-structure before it gets to the time delay. In the LabView block diagram one can find this structure rightmost within the while loop. Without this case-structure the warm up does not start with the set start value. It would begin 0.5 A higher. In general a starting value of 4 A is recommended, because below this value the temperature only rises very slowly.

6.2.6. Cool down

The cool down phase serves the same purpose as the warm up - preventing the basket from thermal strain. The critical temperature range is 300 – 23 °C. The cool down is an optional procedure which can be manually started from a pop up windows when the user stops the program. Beginning from a starting value, entered by the user, the cool down decreases the current successively until 0.5 A are reached.

In the block diagram the functionality can be found right beneath the case structure for warm up/normal operation mode. There are two case structures, one handling the pop up behavior one for calculating the cool down ramp. The cool down ramp has a higher delay between current steps - 320 seconds per default.

Next to the stop button in the block diagram there is a comparison. This terminates the cool down when the calculated current is lower than 0.5 A.

6.2.7. Frontpanel

The front panel, shown in figure 6.3, enables the user to control process parameters and visualizes the current temperature in a diagram. After program start a power supply and the appropriate communication port for the Datalogger can be chosen from the drop down menus. Typically the COM port 6 is the one connected with the Datalogger.

After choosing from the drop down menus, one has to set the option for single- or double basket setup. Depending on the basket setup the recommended starting value for the warm up is 4 A (single basket) or 8 A (double basket).

If these 4 parameters are set, one can click "Connect & Warm Up". A dialog pops up where the user has to confirm, that the water cooling is on. After that, the warm up starts automatically. For the next 90 minutes the warm up mode heats the basket up to a temperature of 300 °C. This is the default warm up temperature and can only be

edited via the block diagram. There is no user control in the frontpanel to change this temperature.

During the warm up phase most control elements are disabled because the user is not meant to influence this phase. When the basket reaches more than 300°C the program activates all control elements and the user can set current, PID output range and PID parameters.

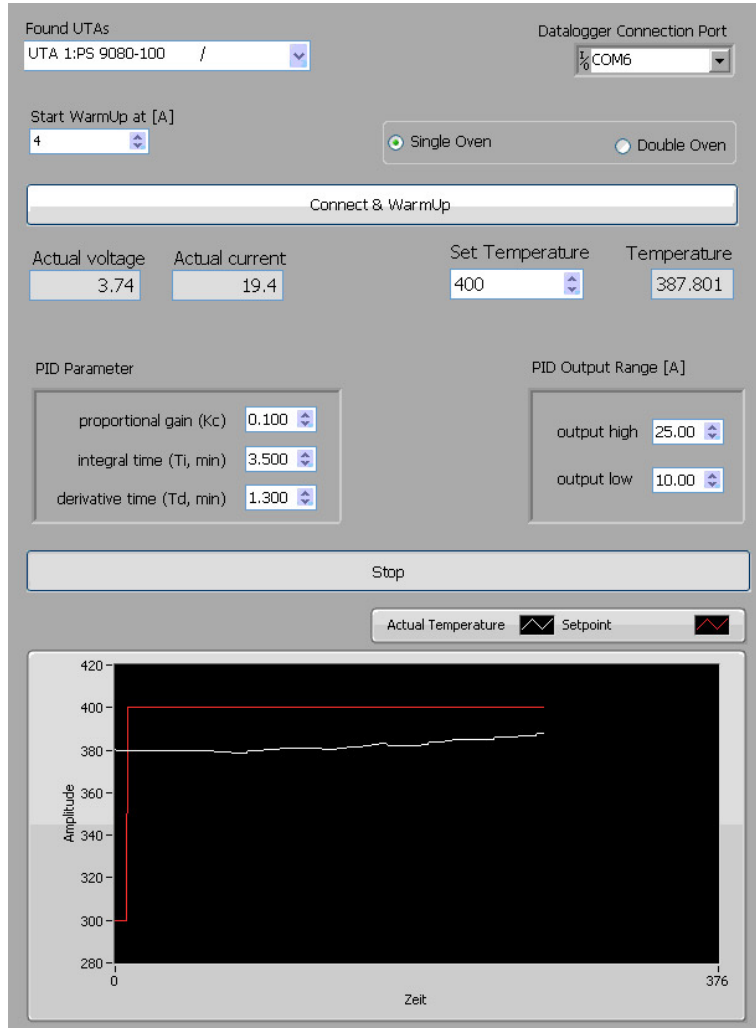


Figure 6.3.: Front panel to control process parameters and visualize the current temperature in the diagram.

6.2.8. Known issues

There are three known issues with the LabView program.

- The program does not check if all devices are connected correctly. Make sure to connect everything properly before starting the program. Otherwise irritating error

messages lead to time consuming troubleshooting.

- Sometimes, even if everything is connected correctly, an error message "No interfaces found..." appears at the start of the application. In that case just try to close LabView and restart it again.
- If someone stops the program manually the current may not be set to zero. In such a case the last value is still preset on the power supply. After stopping check the current manually before leaving the laboratory.

CHAPTER 7

Summary and Conclusion

APPENDIX A

Technical Drawings

APPENDIX B

LabView Block Diagrams

List of Figures

2.1. Helium p - T phase diagram showing ambient pressure in bar over temperature in K. The critical point can be identified at 2.2 bar and 5.3 K. The superfluid phase can be observed at normal pressure below temperatures of $T_\lambda = 2.18$ K. Modified from [3].	5
2.2. The dispersion relation gives the particle energy over the wave vector. Phonon and roton contributions characterize the dispersion relation at different wave vectors. Taken from [3], modified.	6
2.3. Supersonic gas expansion with different velocity regimes expressed in units of M , the Mach number [17]. The zone of silence marks the regime from the nozzle to the mach disk.	8
2.4. Illustration of the beam extraction with a skimmer. The dashed region is the zone of silence [19].	9
2.5. a) Cluster formation within a distance of about 1000 nozzle diameters (5 mm). b) Clusters are cooled further through evaporation of helium atoms. The exponential decay of the cooling rate over time is shown in the diagram. Note that the final temperatures for ^3He and ^4He are very different. [4]	10
2.6. Helium cluster size distribution for $p_a = 80$ bar and different temperatures [24].	11
2.7. The schematic pick up process and dimerization within a helium cluster. Evaporation caused by a pick up process (B) and due to dimerization (D).[28]	12
2.8. The three possibilities to reach $S = 1$ with two electrons. The resulting spin vectors are different in direction but have the same value. Modified from [31].	15
2.9. Fine structure splitting of the helium 2 3P level into three states with energy differences stated in cm^{-1} . [16]	16
2.10. Comparison of harmonic, Morse and a real energy potential (N_2). Modified from [32]	17
2.11. Two electronic states represented by two molecular potentials energy curves with different equilibrium distances R'_e and R''_e . Vibrational and rotational states are drawn within the energy curves. Modified from [33]	18

2.12. Hund's case (a) for a molecule with one valence electron. ℓ and s are independently precessing. The values of their projections are drawn. From [33]	19
2.13. a) Hund's case (c) strong $\mathbf{L} - \mathbf{S}$ interactions. b) Hund's case (a): Independently precessing vectors where the core-field breaks the coupling of \mathbf{L} and \mathbf{S} . From [33]	19
3.1. The three main chambers are shown schematically, with measurement devices and pumps. Taken from [34].	21
3.2. Heat exchanger to cool the high purity helium (spiral wire) and the nozzle to temperatures of about 15 K [35].	23
3.3. The pick up chamber with chopper and available pick up cell types. Beam enters from the right. Taken from [35].	24
3.4. Detection chamber with TOF and QMS mass spectrometer and LIF spectrometer. Modified from [35].	25
3.5. a) TOF in linear mode and b) in reflectron mode. Taken from [35].	26
3.6. Indirect relaxation from an excited state into the vibrational ground state. Taken from [36].	27
3.7. Setup for LIF within the apparatus. Taken from [2].	28
4.1. Example of a REMPI-TOF mass spectrum showing Rb and Sr monomers on the left and dimers on the right. The black graph is the ion yield of the TOF-spectrometer. The green and magenta bars show the contribution of the atoms Rb and Sr respectively, whereas the blue bars represent the RbSr molecule.	30
4.2. Overview of all six peaks within the available spectral range. The gray graph represents the data points whereas the black line corresponds to the smoothed data. Red and blue are the transition probabilities for the Σ and Π states respectively.	31
4.3. Potential energy curves...	32
4.4. The $4^2\Sigma^+ \leftarrow X^2\Sigma^+$ transition in detail. a) REMPI-TOF spectrum. Gray shows the original ion yield, red the smoothed and green the fitted data. The black vertical line marks the onset of the rising edge of the corresponding free molecule transition. b) Shows the LIF spectrum for the transition. c) A comparison of different REMPI-TOF signals to investigate the cause of the background shown in b). The cyan Sr ₂ signal was recorded in a separate experiment.	33
4.5. Gotrian diagram with ground state ($5d^{10}6s\ ^2S_{1/2}$) and first excited state $5d^{10}\ 6p\ ^2P_{1/2}$. All energies correlate to the free atom. ν_1 represents the incident laser photon.	35
4.6. REMPI spectra showing the results for Au (green), AuHe (blue) and AuHe ₂ (red). 2 nm steps. The Indigo-S laser was tuned in steps of 2 nm. The transition from the ground state to the first excited state in the free gold atom is marked.	36

4.7. The spectrum compares the results obtained in 2 nm and 0.6 nm steps for Au (green and magenta). The spectra in 0.6 nm steps are denoted as "fine". Au dimer (Au_2) and trimer (Au_3) are depicted in red and blue, respectively. The energies of possible transitions in this wavelength range are marked.	37
4.8. Comparison of the three spectra for a) Copper [41], b) Silver [40] and c) Gold. The gray line marks the $^2P_{1/2} \leftarrow ^2S_{1/2}$ transition observable for all three elements. The spectra for Au and Ag are REMPI spectra whereas Cu was obtained with a QMS.	39
 5.1. Pick up source with the first basket filled with gold. The second oven is mounted flipped above the first one. The molybdenum ring provides an additional confinement for the gaseous metal. The whole setup is surrounded by a cooling shield in the final setup.	42
5.2. Two-basket setup in the pick up chamber of the apparatus in Cluster Lab III. For illustration purposes without Molybdenum ring.	43
5.3. Fully assembled gold oven with cooling shield and thermocouple. The connectors for the water cooling are made of high quality steel for durability. The brass pipe to align entrance and exit holes is still in place.	44
5.4. Parallel (left) and serial (right) connectors viewed from the back side.	45
 6.1. Problems during basket heating tests. The graph shows heating up and holding current and voltage constant at maximum (1150 °C). Then cooling down to about 800 °C and heating up to 900 °C.	48
6.2. Block diagram of the final LabView program. The stacked sequence structure (film strip) is the outermost frame.	49
6.3. Front panel to control process parameters and visualize the current temperature in the diagram.	54

List of Tables

2.1. <i>Typical values for the mean value and the half width of cluster size distributions at different temperatures. [24]</i>	11
4.1. <i>Possible transitions within the spectral range of the Indigo-S (32000 – 40000 cm⁻¹) for the free atom with respective wavenumbers. From the subtraction in the right column the energies of upper and lower state can be obtained [44].</i>	38
5.1. <i>Adapter to connect the serial port from UTA12 with the parallel port of the power supply. "P" specifies the pin number of the parallel port, "S" the number on the serial port.</i>	45

Bibliography

- [1] LIDE, David R.: *CRC handbook of chemistry and physics*. CRC press, 2004
- [2] LACKNER, Florian: *Laserspektroskopie und Flugzeitmassenspektrometrie an Rubidium-dotierten Heliumnanotröpfchen*, Technische Universität Graz, Institut für Experimentalphysik, Masterarbeit, 2009
- [3] FLIESSBACH, T.: *Statistische Physik, Lehrbuch zur Theoretischen Physik IV*. 5. Auflage. Springer, 2010
- [4] TOENNIES, J. P. ; VILESOV, Andrey F.: Suprafluide Heliumtröpfchen: außergewöhnlich kalte Nanomatrices für Moleküle und molekulare Komplexe. In: *Angew Chem-GER Edit* 116 (2004), Nr. 20, 2674–2702. <http://dx.doi.org/10.1002/ange.200300611>. – DOI 10.1002/ange.200300611. – ISSN 1521–3757
- [5] GREBENEV, Slava ; TOENNIES, J. P. ; VILESOV, Andrei F.: Superfluidity Within a Small Helium-4 Cluster: The Microscopic Andronikashvili Experiment. In: *Science* 279 (1998), Nr. 5359, 2083-2086. <http://dx.doi.org/10.1126/science.279.5359.2083> – DOI 10.1126/science.279.5359.2083
- [6] GREBENEV, Slava ; SARTAKOV, Boris ; TOENNIES, J P. ; VILESOV, Andrei F.: Evidence for superfluidity in para-hydrogen clusters inside helium-4 droplets at 0.15 kelvin. In: *Science* 289 (2000), Nr. 5484, S. 1532–1535
- [7] KINAST, J ; HEMMER, SL ; GEHM, ME ; TURLAPOV, A ; THOMAS, JE: Evidence for superfluidity in a resonantly interacting Fermi gas. In: *Physical review letters* 92 (2004), Nr. 15, S. 150402
- [8] KAPITZA, P: Viscosity of liquid helium below the l-point. In: *Nature* 141 (1938), Nr. 3558, S. 74
- [9] BALIBAR, Sébastien: The discovery of superfluidity. In: *J Low Temp Phys* 146 (2007), Nr. 5-6, S. 441–470

- [10] TISZA, Laszlo: The Theory of Liquid Helium. In: *Phys Rev* 72 (1947), Nov, 838–854. <http://dx.doi.org/10.1103/PhysRev.72.838>. – DOI 10.1103/PhysRev.72.838
- [11] LANDAU, L.: Theory of the Superfluidity of Helium II. In: *Phys Rev* 60 (1941), Aug, 356–358. <http://dx.doi.org/10.1103/PhysRev.60.356>. – DOI 10.1103/PhysRev.60.356
- [12] LEHMANN, Kevin K. ; SCOLES, Giacinto: The ultimate spectroscopic matrix? In: *Science* 279 (1998), Nr. 5359, S. 2065–2066
- [13] SCOLES, G.: *Atomic and Molecular Beam Methods*. Volume 1. Oxford University Press, 1988
- [14] DOAK, RB: *Atomic and Molecular Beam Methods vol 2, ed G Scoles*. New York: Oxford University Press) section, 1992
- [15] TOENNIES, J P. ; VILESOV, Andrej F. ; WHALEY, K B.: Superfluid helium droplets: An ultracold nanolaboratory. In: *Phys Today* 54 (2001), Nr. 2, S. 31–37
- [16] DEMTRÖDER, Wolfgang: *Experimentalphysik 1, Mechanik und Wärme*. 5. Auflage. Springer, 2008
- [17] NAGL, J.: *Aufbau und Test einer Duesenstrahlapparatur zur Spektroskopie an alkalimetall-dotierten Edelgasclustern.*, Technische Universität Graz, Institut für Experimentalphysik, Masterarbeit, 2004
- [18] PAULY, H.: *Atom, Molecule and Cluster Beams I*. Springer, 2000
- [19] CAMPARGUE, R: Progress in overexpanded supersonic jets and skimmed molecular beams in free-jet zones of silence. In: *J Phys Chem-US* 88 (1984), Nr. 20, S. 4466–4474
- [20] STEIN, Gilbert D.: Cluster beam sources: Predictions and limitations of the nucleation theory. In: *Surf Sci* 156 (1985), S. 44–56
- [21] GOYAL, S ; SCHUTT, DL ; SCOLES, G: Infrared spectroscopy in highly quantum matrixes: vibrational spectrum of sulfur hexafluoride ((SF₆) n= 1, 2) attached to helium clusters. In: *J Phys Chem-US* 97 (1993), Nr. 10, S. 2236–2245
- [22] LINDINGER, Albrecht ; TOENNIES, J P. ; VILESOV, Andrej F.: Pump–probe study of the reconstruction of helium surrounding a tetracene molecule inside a helium droplet. In: *Phys Chem Chem Phys* 3 (2001), Nr. 13, S. 2581–2587
- [23] HARMS, Jan ; TOENNIES, J. P. ; DALFOVO, Franco: Density of superfluid helium

- droplets. In: *Phys Rev B* 58 (1998), Aug, 3341–3350. <http://dx.doi.org/10.1103/PhysRevB.58.3341>. – DOI 10.1103/PhysRevB.58.3341
- [24] LEWERENZ, M. ; SCHILLING, B. ; TOENNIES, J.P.: A new scattering deflection method for determining and selecting the sizes of large liquid clusters of 4He. In: *Chem Phys Lett* 206 (1993), 381 - 387. [http://dx.doi.org/http://dx.doi.org/10.1016/0009-2614\(93\)85569-A](http://dx.doi.org/http://dx.doi.org/10.1016/0009-2614(93)85569-A). – DOI [http://dx.doi.org/10.1016/0009-2614\(93\)85569-A](http://dx.doi.org/10.1016/0009-2614(93)85569-A). – ISSN 0009-2614
- [25] LINDEN, Wolfgang von d.: *Wahrscheinlichkeitstheorie, Statistik und Datenanalyse*, Technische Universität Graz, Institut für theoretische Physik, Diplomarbeit, 2002
- [26] LEWERENZ, M. ; SCHILLING, B. ; TOENNIES, J. P.: Successive capture and coagulation of atoms and molecules to small clusters in large liquid helium clusters. In: *J Phys Chem-US* 102 (1995), Nr. 20, 8191-8207. <http://dx.doi.org/http://dx.doi.org/10.1063/1.469231>. – DOI <http://dx.doi.org/10.1063/1.469231>
- [27] BARTELT, A. ; CLOSE, J. D. ; FEDERMANN, F. ; QUAAS, N. ; TOENNIES, J. P.: Cold Metal Clusters: Helium Droplets as a Nanoscale Cryostat. In: *Phys Rev Lett* 77 (1996), Oct, 3525–3528. <http://dx.doi.org/10.1103/PhysRevLett.77.3525>. – DOI 10.1103/PhysRevLett.77.3525
- [28] SCOLES, Giacinto ; LEHMANN, Kevin K.: Nanomatrices Are Cool. In: *Science* 287 (2000), Nr. 5462, 2429-2430. <http://dx.doi.org/10.1126/science.287.5462.2429>. – DOI 10.1126/science.287.5462.2429
- [29] ANCILOTTO, Francesco ; LERNER, PeterB. ; COLE, MiltonW.: Physics of solvation. In: *J Low Temp Phys* 101 (1995), Nr. 5-6, 1123-1146. <http://dx.doi.org/10.1007/BF00754527>. – DOI 10.1007/BF00754527. – ISSN 0022-2291
- [30] MELLA, Massimo ; CALDERONI, Gabriele ; CARGNONI, Fausto: Predicting atomic dopant solvation in helium clusters: The MgHen case. In: *Chem Phys* 123 (2005), Nr. 5, -. <http://dx.doi.org/http://dx.doi.org/10.1063/1.1982787>. – DOI <http://dx.doi.org/10.1063/1.1982787>
- [31] HERTEL, Ingolf V. ; SCHULZ, Claus-Peter: *Atome, Moleküle und optische Physik*. Springer, 2008
- [32] DEMTRÖDER, Wolfgang: *Molekülphysik: theoretische Grundlagen und experimentelle Methoden*. Oldenbourg Verlag, 2013
- [33] DEMTRÖDER, Wolfgang: *Molekülphysik: theoretische Grundlagen und experimentelle Methoden*. Oldenbourg Verlag, 2013
- [34] LACKNER, Florian: *Rydberg States of Alkali-Metal Atoms on Superfluid Helium*

Nanodroplets, Technische Universität Graz, Institut für Experimentalphysik, Doctoral Thesis, 2012

- [35] KROIS, Günter: *Heavy Alkali and Alkaline Earth Metals on Cold Helium Droplets: First Comparision of Excitation Spectra*, Graz University of Technology, Institute of Experimental Physics, Master Thesis, 2011
- [36] DEMTRÖDER, Wolfgang: *Laserspektroskopie*. Bd. 4. Springer, 1993
- [37] KROIS, Günter ; LACKNER, Florian ; POTOTSCHNIG, Johann V. ; BUCHSTEINER, Thomas ; ERNST, Wolfgang E.: Characterization of RbSr Molecules: A Spectral Analysis on Helium Droplets. (2014)
- [38] SPERLING, Ralph A. ; GIL, Pilar R. ; ZHANG, Feng ; ZANELLA, Marco ; PARAK, Wolfgang J.: Biological applications of gold nanoparticles. In: *Chemical Society Reviews* 37 (2008), Nr. 9, S. 1896–1908
- [39] BOISSELIER, Elodie ; ASTRUC, Didier: Gold nanoparticles in nanomedicine: preparations, imaging, diagnostics, therapies and toxicity. In: *Chemical Society Reviews* 38 (2009), Nr. 6, S. 1759–1782
- [40] LOGINOV, Evgeniy ; DRABBELS, Marcel: Excited state dynamics of Ag atoms in helium nanodroplets. In: *The Journal of Physical Chemistry A* 111 (2007), Nr. 31, S. 7504–7515
- [41] LINDEBNER, Friedrich ; KAUTSCH, Andreas ; KOCH, Markus ; ERNST, Wolfgang E.: Laser Ionization and Spectroscopy of Cu in Superfluid Helium Nanodroplets. In: *International Journal of Mass Spectrometry* (2014)
- [42] MOROSHKIN, Peter ; LEBEDEV, V ; WEIS, A: Spectroscopy of gold atoms isolated in liquid and solid ${}^4\text{He}$ matrices. In: *The Journal of chemical physics* 139 (2013), Nr. 10, S. 104307
- [43] PIFRADER, Alexandra: *Pulsed laser spectroscopic investigations of rubidium atoms attached to helium nanodroplets.*, Technische Universität Graz, Institut für Experimentalphysik, Master's thesis, 2009
- [44] <http://physics.nist.gov/>
- [45] http://www.tedpella.com/vacuum_html/vacuum-evaporation-sources.htm
- [46] <http://www.omega.com/temperature/Z/pdf/z241-245.pdf>
- [47] http://www.produktinfo.conrad.com/datenblaetter/100000-124999/100518-da-01-en-Schnittstelle_Voltcraft_K204_Datalogger.pdf

- [48] http://www.elektroautomatik.de/fileadmin/pdf/datasheets/datasheet_uta12.pdf
- [49] http://www.elektroautomatik.de/fileadmin/pdf/datasheets/datasheet_ps9000.pdf
- [50] <http://www.omega.com/temperature/Z/pdf/z198-201.pdf>
- [51] <http://www.omega.de/pdf/tc/z204-205iec.pdf>

Acknowledgments
